EFFECT OF BIAXIAL STRAIN ON THE PERFORMANCE OF GRAPHENE/BN HETERO BILAYER BASED FIELD EFFECT TRANSISTOR

A thesis submitted in partial fulfillment of the requirement for the degree
of
Master of Science in Electrical and Electronic Engineering

by

Md. Hasibul Alam

STUDENT NUMBER 0412062224

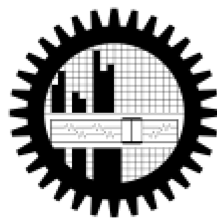

Department of Electrical and Electronic Engineering

Bangladesh University of Engineering and Technology

Dhaka-1000

September, 2014

Certification

The thesis titled **"EFFECT OF BIAXIAL STRAIN ON THE PERFORMANCE OF GRAPHENE/BN HETERO BILAYER BASED FIELD EFFECT TRANSISTOR"** submitted by Md. Hasibul Alam, Student No: 0412062224, Session: April, 2012, has been accepted as satisfactory in partial fulfillment of the requirement for the degree of MASTER OF SCIENCE IN ELECTRICAL AND ELECTRONIC ENGINEERING on September 30, 2014.

BOARD OF EXAMINERS

1. ____

Dr. Quazi Deen Mohd Khosru — Chairman (Supervisor)
Professor
Department of Electrical and Electronic Engineering,
Bangladesh University of Engineering and Technology,
Dhaka – 1000, Bangladesh.

2. ____

Dr. Taifur Ahmed Chowdhury — Member (Ex-officio)
Professor and Head
Department of Electrical and Electronic Engineering,
Bangladesh University of Engineering and Technology,
Dhaka – 1000, Bangladesh.

3. ____

Dr. Samia Subrina — Member
Associate Professor
Department of Electrical and Electronic Engineering,
Bangladesh University of Engineering and Technology,
Dhaka – 1000, Bangladesh.

4. ____

Dr. Zahid Hasan Mahmood — Member (External)
Professor
Department of Applied Physics, Electronics and Communication Engineering,
University of Dhaka,
Dhaka-1000, Bangladesh.

Declaration

It is hereby declared that this thesis or any part of it has not been submitted elsewhere for the award of any degree or diploma and that all sources are acknowledged.

Signature of the Candidate

____

Md. Hasibul Alam

To my beloved parents

Acknowledgment

First of all, I would like to thank Almighty for giving me the strength and patience to complete this thesis.

I would then like to express my sincere gratitude to my thesis supervisor, Dr. Quazi Deen Mohd Khosru, Professor, Department of Electrical and Electronic Engineering, BUET, for his generous help, encouragement and support throughout my thesis. Whenever I faced problems and didn't know how to proceed, he pointed me to the right direction.

I would also like to thank the other members of the thesis committee for taking the time to evaluate my work. I am also especially thankful to the current head of EEE department, Prof. Taifur Ahmed Chowdhury and the past head, Prof. Pran Kahai Saha for their support during my thesis work.

I also express my gratitude to my friends who often helped me throughout my work. Many of the discussions I had with them gave me new ideas about new approaches towards my work.

Last, but not the least, I thank my parents and dedicate my thesis to them. They have helped me in every way possible throughout this journey. This thesis work would not have been possible without their help.

Abstract

Recent simulation study shows that a considerable and stable band gap can be opened in 2D materials by applying biaxial strain. But a systematic study on the effect of biaxial strain on band gap and other important material electronic parameters are still missing in literature. In this thesis, the structural and electronic properties of various configurations of graphene/hexagonal Boron Nitride hetero bilayer (C/h-BN HBL) system has been investigated using density functional theory (DFT) under local density approximation (LDA).Biaxial strain has been applied on this material and its effect on electronic band structure and properties derived from band structure such band gap, carrier effective mass, Fermi velocity have also been simulated. This work reveals that irrespective of the application of biaxial strain it remains direct and hence can be exploited in optoelectronic applications. Also, it has been observed that the band gap increases monotonically (29.7meV-113.4meV) from compressive to tensile strain region. The electron effective mass (0.003732m_e-0.024902 m_e) and hole effective mass (0.003747 me-0.023888 me) also increases from compressive to tensile strain region. But Fermi velocity for both electron (1.257278×10^6 m/s-0.3866997×10^6 m/s) and hole (1.265725×10^6 m/s-0.3816452×10^6 m/s) shows an opposite trend. From density of states (DOS) it is clear that this material system shows a linear trend in lower energy region as observed in pristine graphene. Band structure calculation shows an almost linear dispersion relationship at Dirac point which predicts the Fermion like characteristics of electrons in this material system. Finally, biaxial strained materials were implemented in the channel of a top gate ballistic MOSFET and device performance was investigated using non-equilibrium Green's function (NEGF) coupled with DFT. The results show that for lower band gap material the transport lacks saturation region which is crucial for stable operation of transistors in logic circuits. It is also obvious from the results that carrier effective mass and Fermi velocity has negligible effect on drive current. Ultimately, an optimum channel material (12% tensile strained B3 configuration) was proposed and implemented in the channel of MOSFET. Better device performance with current saturation has been observed with this proposed material.

CONTENTS

LIST OF TABLES ix
LIST OF FIGURES x

1. Introduction 1
1. 1 Preface 1
1. 2 Literature Review 2
1. 3 Thesis Objective 6
1. 4 Thesis Organization 7
2. Theoretical Background 8
2. 1 Density Functional Theory 8
2.1.1 Introduction 8
2.1.2 Hohenberg-Kohn Theorems 10
2.1.3 Kohn-Sham Equations 10
2.1.4 Exchange-correlation functional 11
2.1.5 Hellmann-Feynman Theorem 13
2.1.6 Plane wave basis and Pseudo potential 14
2.1.6.1 Plane wave basis 14
2.1.6.2 Pseudo potentials 16
2. 2 Non-Equilibrium Green's Functions 16
2.2.1 Non Equilibrium Electron Distribution 16
2.2.2 Electron Density Matrix 17
2.2.3 Retarded Green's Function 18
2.2.4 Spill-In Terms 19
2.2.5 Effective Potential 19
2.2.6 Transmission Coefficient 20
3. Model and Computational Details 22
3.1 Graphene/Hexagonal Boron Nitride Bilayer System 22
3.2 Computational Details 23
3.3 Methodology 24

3.3.1 Effective Mass 24
3.3.2 Fermi Velocity 25
3.3.3 IV Characteristics 25
3.3.4 Model Validation 26
4. Results and Discussion: Material Properties 28
4.1 Atomic Structure and Geometry Optimization 28
4.2 Electronic Structure 31
4.2.1 Band Structure 31
4.2.2 Density of States 33
4.3 Effect of Biaxial Strain 35
4.3.1 Band Structure 35
4.3.2 DOS 40
4.3.3 Band Gap 47
4.3.4 Effective Mass 48
4.3.4.1 Electron Effective Mass 49
4.3.4.2 Hole Effective Mass 49
4.3.5 Fermi Velocity 51
4.3.5.1 Electron Fermi Velocity 51
4.3.5.2 Hole Fermi Velocity 52
5 Transport Performance: Ballistic MOSFET 53
5.1 Basic Device Structure 53
5.2 IV Characteristics 54
5.2.1 Effect of Strain (B1 Configuration) 55
5.2.2 Effect of Strain (B2 Configuration) 55
5.2.3 Effect of Strain (B3 Configuration) 56
5.3 Optimum Channel Material for Ballistic MOSFET 57
6 Conclusion 59
6.1 Summary 59
6.2 Suggestion for Future Work 60

References 61
Appendix A 71

LIST OF TABLES

3.1 Lattice Parameter and band gap for B1 26

LIST OF FIGURES

3.1(a)	B1 Top	22
3.1(b)	B1 Upside	22
3.2 (a)	B2 Top	23
3.2 (b)	B2 Upside	23
3.3 (a)	B3 Top	23
3.3 (b)	B3 Upside	23
3.4	The band gap of B1 structure as a function of biaxial strain applied to the super lattice. The red line shows the results obtained in this work and the green line is obtained from the result published by G. Mukhopadhyay *et al.*[63]	26
3.5	Longitudinal electron effective mass of B1 structure as a function of biaxial strain. Result published by G. Mukhopadhyay *et al.* [63] using Eq. (3.2) is shown in blue line. Electron effective mass calculated using Eq. (3.1) in this work is shown in red line.	27
4.1	The total energy of B1 structure as a function of lattice parameter and interlayer distance	29
4.2	The total energy of B2 structure as a function of lattice parameter and interlayer distance	30
4.3	The total energy of B3 structure as a function of lattice parameter and interlayer distance.	30
4.4	Band structure for optimized structure of B1 configuration	31
4.5	Band structure for optimized structure of B2 configuration	32
4.6	Band structure for optimized structure of B3 configuration	32
4.7	DOS for optimized structure of B1	34
4.8	DOS for optimized structure of B2	34
4.9	DOS for optimized structure of B3	34
4.10	The band structures of the strained super lattice (B1 configuration). A to E shows the band structure of super lattice when +2.4%, +4.8%, +7.2%, +9.6% and +12% strain was applied. F to J shows the band structure when the super lattice was compressed to 2.4%, 4.8%, 7.2%, 9.6% and 12% respectively	36
4.11	Effect of biaxial strain on the band structure of B1 conduction band (top) valence band (bottom)	37
4.12	The band structures of the strained super lattice (B2 configuration). A to E shows the band structure of super lattice when +2.4%, +4.8%, +7.2%, +9.6% and +12% strain was	38

applied. F to J shows the band structure when the super lattice was compressed to 2.4%, 4.8%, 7.2%, 9.6% and 12% respectively

4.13 The band structures of the strained super lattice (B3 configuration). A to E shows the band structure of super lattice when +2.4%, +4.8%, +7.2%, +9.6% and +12% strain was applied. F to J shows the band structure when the super lattice was compressed to 2.4%, 4.8%, 7.2%, 9.6% and 12% respectively 39

4.14 The DOS of the strained super lattice (B1 configuration). A to E shows the band structure of super lattice when +2.4%, +4.8%, +7.2%, +9.6% and +12% strain was applied. F to J shows the band structure when the super lattice was compressed to 2.4%, 4.8%, 7.2%, 9.6% and 12% respectively 41

4.15 The integrated DOS of the strained super lattice (B1 configuration). A to E shows the band structure of super lattice when +2.4%, +4.8%, +7.2%, +9.6% and +12% strain was applied. F to J shows the band structure when the super lattice was compressed to 2.4%, 4.8%, 7.2%, 9.6% and 12% respectively 42

4.16 The DOS of the strained super lattice (B2 configuration). A to E shows the band structure of super lattice when +2.4%, +4.8%, +7.2%, +9.6% and +12% strain was applied. F to J shows the band structure when the super lattice was compressed to 2.4%, 4.8%, 7.2%, 9.6% and 12% respectively 43

4.17 The integrated DOS of the strained super lattice (B2 configuration). A to E shows the band structure of super lattice when +2.4%, +4.8%, +7.2%, +9.6% and +12% strain was applied. F to J shows the band structure when the super lattice was compressed to 2.4%, 4.8%, 7.2%, 9.6% and 12% respectively 44

4.18 The DOS of the strained super lattice (B3 configuration). A to E shows the band structure of super lattice when +2.4%, +4.8%, +7.2%, +9.6% and +12% strain was applied. F to J shows the band structure when the super lattice was compressed to 2.4%, 4.8%, 7.2%, 9.6% and 12% respectively 45

4.19 The integrated DOS of the strained super lattice (B3 configuration). A to E shows the band structure of super lattice when +2.4%, +4.8%, +7.2%, +9.6% and +12% strain was applied. F to J shows the band structure when the super lattice was compressed to 2.4%, 4.8%, 7.2%, 9.6% and 12% respectively 46

4.20 The band gap of B1, B2 and B3 as a function of percentage biaxial strain applied to the super lattice 47

4.21 Longitudinal electron effective mass of B1, B2 and B3 as a function of percentage biaxial strain applied to the super lattice. 48

4.22	Transverse electron effective mass of B1, B2 and B3 as a function of percentage biaxial strain applied to the super lattice	49
4.23	Longitudinal hole effective mass of B1, B2 and B3 as a function of percentage biaxial strain applied to the super lattice	50
4.24	Transverse hole effective mass of B1, B2 and B3 as a function of percentage biaxial strain applied to the super lattice	50
4.25	Electron Fermi velocity of B1, B2 and B3 as a function of percentage biaxial strain applied to the super lattice	51
4.26	Hole Fermi velocity of B1, B2 and B3 as a function of percentage biaxial strain applied to the super lattice	52
5.1	Basic device structure of C/h-BN channel ballistic MOSFET	53
5.2	Basic device structure of C/h-BN channel ballistic MOSFET	54
5.3	IV characteristics curve for relaxed structures of B1, B2 and B3	54
5.4	Effect of biaxial strain on I-V characteristics for B1 configuration based MOSFET	55
5.5	Effect of biaxial strain on I-V characteristics for B2 configuration based MOSFET	56
5.6	Effect of biaxial strain on I-V characteristics for B3 configuration based MOSFET	57
5.7	Drain current at a particular drain voltage is plotted as a function of percentage biaxial strain. Here V_{DS}=0.5V	58
5.8	IV characteristics curve with proposed material in channel of MOSFET	58
A.1	A flow chart of Kohn-Sham equation algorithm	71

Chapter 1

Introduction

1.1 Preface

The dimensions of modern silicon metal-oxide semiconductor field-effect transistors (MOSFETs) have been shrinking exponentially with the prediction of Moore's law. This scaling produces transistor faster than the previous generation but requires more power density. The conventional planar structures become less efficient in heat management as the critical thickness of the channel decreases. Moreover, FETs with short gates frequently suffer from degraded electrostatics and short channel effects such as threshold voltage roll-off, drain induced barrier lowering and impaired drain current saturation [1]-[4]. This is because the gate gradually loses control over the channel and is not as efficient in switching off the channel. Consequently, it gives rise to huge power consumption because much leakage current passes through the transistors even when they are at the "off" state. This has been one of the major issues preventing further scaling down of MOSFETs. In order to minimize such effects, many new approaches have been implemented based on silicon technology, including the use of high-k dielectrics [5] and multiple gates [6] to better switch off the devices. On the other hand, people have also been seeking other materials to complement or even replace silicon technology.

Scaling theory predicts that a FET with a thin barrier and a thin gate-controlled region will be robust against short-channel effects down to very short gate lengths [7].The possibility of having channels that are just one atomic layer thick is perhaps the most attractive feature of graphene for use in transistors. By comparison, the channels in III–V HEMTs are typically 10–15 nm thick, and although silicon-on-insulator MOSFETs with channel thicknesses of less than 2 nm have been reported, rough interfaces caused their

mobility to deteriorate. More importantly, the body of these MOSFETs showed thickness fluctuations that will lead to unacceptably large threshold-voltage variations. Similar problems are expected to occur when the thickness of the channel in III–V HEMT is reduced to only a few nanometers. These problems occur at thicknesses that are many times greater than the thickness of graphene [8].

Although graphene is a promising candidate for next generation electronics, the unique electronic structure is actually not ideal for logic device applications. Graphene does not have a band gap, so at finite temperature, electrons are thermally excited to the conduction band. As a result, graphene transistors usually have an on/off ratio lower than 10 at room temperature, far below the requirement for logic applications.

However, the band structure of graphene can be modified, and it is possible to open a band gap in several ways [9]-[22].

Once the problem of creating band gap is resolved in graphene, there comes the issue of substrate related mobility degradation due to surface phonon scattering, charge doping and surface roughness on SiO_2/Si substrate [23]. Recently, graphene on hexagonal boron nitride (h-BN) has shown enhanced mobility, reduced carrier inhomogeneity and reduced intrinsic doping than on SiO_2 [24]. So to reduce SiO_2/Si substrate induced performance degradation, graphene/h-BN hetero bilayer composite material can be a promising channel material for future logic FETs.

1.2 Literature Review

The lattice structure of the purely two dimensional single-layer graphene consists of regular hexagons with a carbon atom at each corner. Although the idea was introduced in reports decades ago, even before the name graphene had been coined [25]–[27], but it was only after the publication of the 2004 paper by the Manchester group [28] that veered attention of most researchers towards this field.

The devices with channels made of large-area graphene, a semimetal with zero band gap, cannot be switched off and therefore are not suitable for logic applications. However, by modifying the band structure of graphene it is possible to open a band gap in three ways:

- by constraining large-area graphene in one dimension to form graphene nanoribbons, [9]-[11]
- by biasing bilayer graphene [12]-[15]
- by applying strain to graphene [16]-[19]

It has been predicted that both armchair nanoribbons and zigzag nanoribbons have a band gap that is inversely proportional to the width of the nanoribbon [29]. The opening of a band gap in nanoribbons has been verified experimentally for widths as low as about 1 nm [9],[30]-[32], and theory and experiments both reveal band gaps in excess of 200 meV for widths below 20 nm. However, it should be noted that real nanoribbons have rough edges and widths that change along their lengths. Even modest edge disorder obliterates any difference in the band gap between nanoribbons with different edge geometries [10], as well as edge functionalization and doping can also affect the band gap [11].

To open a band gap useful for conventional field-effect devices, very narrow nanoribbons with well-defined edges are needed. But owing to the limitation of availability of necessary equipments currently, this poses a serious challenge. Although nanoribbons with uniform width and reduced edge roughness were produced by ‘unzipping’ carbon nanotubes [33], even a perfect nanoribbon is not perfect for electronics applications. In general, the larger the band gap that opens in a nanoribbon, the more the valence and conduction bands become parabolic (rather than cone-shaped): this decreases the curvature around the K point and increases the effective mass of the charge carriers [34] , which in turn decreases the mobility.

Bilayer graphene, which is also gapless, has its valence and conduction bands assume a parabolic shape near the K point. If, however, an electric field is applied perpendicular to

the bilayer, a band gap opens and the bands near the K point take on the so-called Mexican-hat shape. This opening was not only predicted by theory, where investigations have shown the size of the band gap to depends on the strength of the perpendicular field and to reach values of 200–250 meV for high fields ((1–3) × 10^7 V cm^{-1} [12]-[13], but has also been verified in experiments [14]-[15].

Finally, strain is discussed as a means of opening a band gap in large-area graphene, and the effect of uniaxial strain on the band structure is simulated [20],[35]. Currently, it seems, if possible at all, opening a gap in this way will require a global uniaxial strain exceeding 20%, which is difficult to achieve in practice. Moreover, little is known about the ways in which other types of strain, such as biaxial strain influence the band structure of graphene.

In addition to the aforementioned limitation, there are some other issues that need consideration. Various properties of graphene depend highly on surface and interfaces, which, on one hand, can be exploited to engineer the graphene, such as doping, but on the other hand, such actions inevitably introduce extra scattering. SiO_2, the most commonly used substrate for graphene devices, has been found to have room temperature mobility limited by surface phonons to ~4×10^4 cm^2/V.s, much inferior to the intrinsic limit [23], which is in reality, further degraded to less than 1×10^4 cm^2/V.s by charged impurities and surface roughness on the substrate [36].Such degradation highlights the importance of interface engineering in graphene.

Hexagonal boron nitride (h-BN) has been reported as an ideal substrate for graphene because of its atomic flatness, absence of charge traps, and large optical phonon modes, and hence leading to a reduction in carrier scattering in graphene [24].Dean *et al.* [24] first demonstrated a dry transfer process to place graphene on h-BN flakes on a SiO_2/Si substrate during which the side of graphene facing h-BN was never in contact with any liquid, so as to preserve the original nature of the interface, which turned out to be very

important. AFM and STM characterizations indicated that graphene is much flatter on h-BN than on SiO_2 and much more homogeneous [37]. So far, graphene sandwiched between h-BN offers the cleanest sample on any substrate, where many exciting quantum states have been observed, including fractional quantum Hall states[38], quantum Hall iso-spin ferromagnetic states[39],and Hofstadter spectra [40]–[42].

Recent experiments [43]-[44] at Columbia University have shown successful fabrication of hexagonal BN (h-BN) gated graphene field effect transistors (BN-GFETs), that includes both mono-layer graphene (MLG) and bilayer graphene (BLG) on h-BN gate/substrate which could be made arbitrarily thin and are considered to be among the important developments in the physics and material science of graphene [45]–[47]. Graphene supported on h-BN exhibits superior electrical properties with performance levels comparable to those observed in suspended samples [43], [44], [46], [47].Besides, in the context of strain engineering of electronic properties of graphene, another experimental development [48] uses piezoelectric actuators to apply tunable biaxial compressive as well as tensile stresses to graphene on h-BN substrate, which allows a detailed study of the interplay between the graphene geometrical structures and its electronic properties

Previous theoretical studies on graphene on h-BN substrate [50] and C/h-BN HBL [49]-[51] reported the opening of a small energy band gap in graphene which varies with the following:

(a) the stacking order,
(b) the separation distance of graphene from the h-BN, and
(c) the externally applied perpendicular electric field.

Other graphene/h-BN hetero structures such as MLG [50] and BLG [51] sandwiched between two mono-layers of h-BN have also been theoretically shown to have (external)

electric-field-tunable electronic properties. Various strain distributions on mono-layer h-BN [53] and graphene [54]–[57] have been reported recently. Theoretically it is shown that the high band gap of mono-layer h-BN is strain-tunable [52], the gap-less nature of graphene is robust against small and moderate deformations [53]–[56]. On the experimental side, Raman spectroscopy studies of graphene reveal that both biaxial [56] and uniaxial [57]–[59] strains affect the Raman Peaks; the transport properties of strained graphene have been investigated by depositing samples on stretchable substrates [60]-[62]. Behera *et al*. [63] reported strain engineered band gap for one of the configurations of C/h-BN HBL. Again, biaxial strain has also been applied on C/h-BN HBL experimentally [22]. But a detailed systematic simulation of biaxial strain-engineered electronic properties such as band structure, band gap, carrier effective mass and Fermi velocity is yet to be reported for all the configurations of C/h-BN HBL to the best of our knowledge. Moreover, tailoring the biaxial strain dependent band gap of C/h-BN in logic transistor and investigating the transport phenomena have not been undertaken yet to the best of our knowledge.

1.3 Thesis Objective

The primary objective of this work is to perform relaxation by allowing all the atoms in the unit cell to move freely until the optimized structure in equilibrium is obtained and to apply biaxial strain in the composite material and relax the structure. In addition to that, calculation of the band structure of both the equilibrium and strained structures of graphene/h-BN hetero bilayer material using Density Functional Theory (DFT) is also shown. And, finally, this proposed material is applied as channel in a ballistic top gate transistor and the transistor transport performance was investigated.

In this thesis, hexagonal structure of graphene with the lattice parameter reported in [49] will be used as a starting point for geometry relaxation of C/h-BN HBL structure. The geometry relaxations will be performed by computing the Hellmann–Feynman (H–F)

forces using conjugate gradient algorithm [64]. All atoms in the unit cell will be allowed to move freely until the H–F force on each atom is smaller than 0.001 eVÅ^{-1}. After geometry relaxation optimized structure will be obtained. Biaxial compressive and tensile strain will then be applied on bilayer C/h-BN HBL by changing the in-plane (a and b, equally) cell parameters, relaxing the structure along the direction perpendicular to the sheet since on applying an in-plane biaxial strain a deformation in the perpendicular direction is likely. Hence, interlayer distance of the relaxed structure will be obtained for various strain values. First-principles calculation will be performed to investigate biaxial strain dependent electronic properties of the bilayer material. The first-principles calculations will be performed within the density-functional theory (DFT) using plane wave basis set. Perdew-Zunger variant LDA (Local Density Approximation) will be performed using the Ab initio code PWSCF package of Quantum Espresso [65]. To include the electron-ion interaction norm conservative pseudo potentials will be used for all the atoms. Finally, the newly proposed channel material will be implemented in a top gate ballistic MOSFET and biaxial strain dependent transport performance will be investigated by the DFT coupled with Non-Equilibrium Green's Function (NEGF) formalism [66]-[67].

1.4 Thesis Organization

Theory behind calculation of material electronic parameters and transport phenomena is discussed in Chapter 2 whereas Chapter 3 deals with computational details and methodologies. Chapter 4 contains the detailed results of the electrical properties of the proposed material. Then the results of the transport phenomena with respect to biaxial strain are interpreted in Chapter 5. Finally, the conclusions are drawn in Chapter 6 as well as suggestions for future improvements are proposed.

Chapter 2

Theoretical Background

Density functional theory (DFT) which lies behind the structural and electronic properties simulation of material is discussed thoroughly in this chapter. Moreover, Non Equilibrium Green's Function (NEGF) Technique which is widely used in couple with DFT to investigate transport properties of ballistic transistors is also discussed in this chapter.

2.1 Density Functional Theory (DFT)

2.1.1 Introduction

Since electrons are thousand times lighter than the nuclei, the nuclei can be treated as a static point charge known as the Born-Oppenheimer approximation [68]. This assumption greatly simplifies the problem of interacting electrons with nuclei and makes the electronic Hamiltonian of the solid as follows:

$$H = T + V_{ee} + V_{ei} \tag{2.1}$$

Where

T= kinetic energy of electrons of mass m

V_{ee}= repulsive interaction between electrons

V_{ei} =attractive interaction between electrons and ions

And

$$T = -\frac{\hbar^2}{2m}\sum_i \nabla_i^2 \quad (2.2)$$

$$V_{ee} = \frac{1}{2}\sum_{i\neq j}\frac{e^2}{|r_i - r_j|} \quad (2.3)$$

$$V_{ei} = \sum_i V_{ion}(r_i) = -\sum_{iI}\frac{Z_I e^2}{|r_i - R_I|} \quad (2.4)$$

Where,

e = the quantum of charge

$\{R_I\}$= the positions of fixed nuclei

r_i= position of electron

The electron density is defined as follows:

$$n(\mathbf{r}) = N\int d\mathbf{r}_2 \ldots . d\mathbf{r}_N |\psi(\mathbf{r}, \mathbf{r}_2 \ldots . \mathbf{r}_N)|^2 \quad (2.5)$$

Where

N=the number of electrons

Ψ (r_1, r_2, ..., r_N)= Eigen function of H.

For the ground state of H, the Eigen function is denoted by Ψ_0 and its associated electron density is n_0(r) defined by Eq. (2.5). Eq. (2.1) should be solved for n(r) instead of ψ(r) self consistently.

2.1.2 Hohenberg-Kohn Theorems

It is formidable to directly solve the Schrödinger's equation of the solid Hamiltonian of Eq. (2.1). To solve this problem, Hohenberg and Kohn [69] proposed an alternative to the ground state solution. It is based on two theorems:

Theorem I: Up to a trivial additive constant, the ionic potential $V_{ion}(r)$ has a one-to-one correspondence to the ground state electron density $n_0(r)$, that is different ionic potentials must have different ground state electron densities.

Theorem II: For a given ionic potential $V_{ion}(r)$, we define an energy functional $E[n]$ as

$$E[n] = \int d\mathbf{r} n(\mathbf{r}) V_{ext}(\mathbf{r}) + F[n] \tag{2.6}$$

This functional takes its minimum value at the ground state electron density $n_0(r)$ and its value is the ground state energy E_0.

2.1.3 Kohn-Sham Equations

Kohn-Sham equations [70], the basis of Kohn-Sham density functional theory, are derived by forcing identical ground state electron density and assuming same external potential for both a many-electron interacting system and a non-interacting system. We can first write out the energy functional in Eq. (2.6) as:

$$E[n(\mathbf{r})] = -\frac{\hbar^2}{2m}\sum_i \langle\psi_i|\nabla^2||\psi_i|\rangle + \frac{e^2}{2}\iint d\mathbf{r}d\mathbf{r}'\frac{n(\mathbf{r})n(\mathbf{r}')}{|\mathbf{r}-\mathbf{r}'|} + E_{xc}[n(\mathbf{r})] + \int d\mathbf{r} n(\mathbf{r}) V_{ion}(\mathbf{r}) \tag{2.7}$$

Where the electron density is constructed as:

$$n(\mathbf{r}) = \sum_i |\psi_i(\mathbf{r})|^2 \tag{2.8}$$

Here i refers to single-particle states and the sum is over all the occupied states. $E_{xc}[n(r)]$ is called exchange-correlation functional, which is whatever is left to make Eq. (2.7) exact. Taking functional derivative $\delta E[n(r)]/\delta\psi_i^*(\mathrm{r})$ with the constraint that each $\psi_i(\mathrm{r})$ is normalized to unit leads to:

$$\left(-\frac{\hbar^2}{2m}\nabla^2 + V_{KS}\right)\psi_i(\mathbf{r}) = \epsilon_i\psi_i(\mathbf{r}) \tag{2.9}$$

Where $V_{KS}(\mathbf{r})$ is composed of:

$$V_{KS}(\mathbf{r}) = \int d\mathbf{r}'\,\frac{n(\mathbf{r}')}{|\mathbf{r}-\mathbf{r}'|} + V_{ion}(\mathbf{r}) + V_{xc}(\mathbf{r}) \tag{2.10}$$

The first term is the Hartree potential and denoted by V_H. The second term is the local ionic potential. The last term is the exchange-correlation potential which is defined as:

$$V_{xc}(\mathbf{r}) = \frac{\delta E_{xc}[n]}{\delta n(\mathbf{r})} \tag{2.11}$$

Once the equations Eq. (2.9-2.11) are solved self-consistently (the solutions are denoted by $\{\tilde{\psi}_i\}$), we obtain the ground state electron density:

$$n_o(\mathbf{r}) = \sum_i\left|\tilde{\psi}_i(\mathbf{r})\right|^2 \tag{2.12}$$

And ground state energy:

$$E_o = -\frac{\hbar^2}{2m}\sum_i\langle\widetilde{\psi_i}|\nabla^2||\widetilde{\psi_i}|\rangle + \frac{e^2}{2}\iint d\mathbf{r}d\mathbf{r}'\,\frac{n_o(\mathbf{r})n_o(\mathbf{r}')}{|\mathbf{r}-\mathbf{r}'|} + E_{xc}[n_o] + \int d\mathbf{r}n_{\mathbf{o}}(\mathbf{r})V_{ion}(\mathbf{r}) \tag{2.13}$$

2.1.4 Exchange-correlation functional

The exact form of exchange-correlation functional is unknown. Various approximations have been made. The most widely used approximations in the solid-state calculations are

Local Density Approximation (LDA) [71] and Generalized Gradient Approximation (GGA) [72]-[73], and the former one was used in this work. So, detailed description of it is provided here. In this approximation, one models each small region of space around r as a uniform electron gas at the electron density *n(r)*.

$$E_{xc}[n] \simeq E_{xc}^{LDA} = \int d\mathbf{r}n(\mathbf{r})\varepsilon_{xc}(n(\mathbf{r})) \tag{2.14}$$

Where ε_{xc}(n) is the exchange-correlation energy per atom in a uniform density at n. However ε_{xc}(n) cannot be calculated analytically. Usually ε_{xc}(n) is decomposed into exchange part and correlation part:

$$\varepsilon_{xc}(n) = \varepsilon_x(n) + \varepsilon_c(n) \tag{2.15}$$

For a uniform distributed electron gas, using the Hartree-Fock approximation, the exchange energy can analytically be calculated [74]:

$$\varepsilon_x(n) = -\frac{3e^2}{4\pi}(3\pi^2 n)^{1/3} \tag{2.16}$$

The correlation part is more difficult to calculate analytically. In the high density limit ($r_s << a_0$), we have the following serial expansion from many body perturbation theory in the unit of Ry:

$$\varepsilon_c(n) = 0.0622\ln(r_s/a_o) - 0.096 + O(r_s/a_o) \tag{2.17}$$

The most important result is the Ceperley and Alder monte carlo calculations that numerically computed the correlation part to high accuracy. Based on that, Perdew and Zunger further parametrize the ε_c(n) [71] as

$$\varepsilon_c(n) = \begin{cases} 0.0622\ln\left(\frac{r_s}{a_0}\right) - 0.096 + O\left(\frac{r_s}{a_o}\right)\ln\left(\frac{r_s}{a_0}\right) - 0.0232\left(\frac{r_s}{a_0}\right) & (r_s < a_0) \\ -0.2846(1 + 1.0529\sqrt{\left(\frac{r_s}{a_o}\right)} + 0.3334\left(\frac{r_s}{a_o}\right))^{-1} & (r_s > a_0) \end{cases} \tag{2.18}$$

The exchange-correlation potential of LDA follows from Eq.(2.11) and Eq. (2.14):

$$V_{xc}^{LDA}(\mathbf{r}) = \frac{\delta E_{xc}^{LDA}[n]}{\delta n(\mathbf{r})} = \frac{d[n\varepsilon_{xc}(n)]}{dn}\bigg|_{n(\mathbf{r})} \quad (2.19)$$

2.1.5 Hellmann-Feynman theorem

For a given ion configuration, the Kohn-Sham equations calculate the self-consistent electron density for the ground state. The total energy for the ground state is given by Eq. (2.13).

The force on the ion I is by definition:

$$F_I = -\frac{\partial}{\partial R_I}(E_o + E_{ii}) \quad (2.20)$$

E_{ii}= ion-ion interaction energy

The second term is straightforward, though the explicit expression could be complicated. The tricky term is the first one, in which V_{ion} (given by Eq. (2.4)) explicitly depends on R_I but the Kohn-Sham states $\{\psi_i\}$ implicitly depend on the R_I. Therefore when we take the full derivative, we have three contributions:

$$\frac{\partial E_o}{\partial R_I} = \frac{\partial E_o}{\partial R_I}\bigg|_{\{\tilde{\psi}_i\}} + \sum_i \int d\mathbf{r} \left\{ \frac{\delta E_o}{\delta \tilde{\psi}_i^*(\mathbf{r})} \frac{\partial \tilde{\psi}_i^*(\mathbf{r})}{\partial R_I} + \frac{\delta E_o}{\delta \tilde{\psi}_i(\mathbf{r})} \frac{\partial \tilde{\psi}_i(\mathbf{r})}{\partial R_I} \right\} \quad (2.21)$$

We can see that the functional derivative $\delta E_0/\delta\psi_i^*(\mathrm{r})$ gives the Kohn-Sham equations:

$$\frac{\delta E_o}{\delta \tilde{\psi}_i^*(\mathbf{r})} = \left[-\frac{\hbar}{2m}\nabla^2 + V_{ion}(\mathbf{r}) + \int d\mathbf{r}' \frac{n(\mathbf{r}')}{|\mathbf{r}-\mathbf{r}'|} + V_{xc}(\mathbf{r}) \right] \tilde{\psi}_i(\mathbf{r}) = \epsilon_i \tilde{\psi}_i(\mathbf{r}) \quad (2.22)$$

The second equality holds because $\{\psi_i\}$ are a set of solutions to the Kohn-Sham equations. By taking the complex conjugate, we obtain:

$$\frac{\partial E_o}{\partial R_I} = \frac{\partial E_o}{\partial R_I}\bigg|_{\{\tilde{\psi}_i\}} + \sum_i \int d\mathbf{r} \left\{ \epsilon_i \tilde{\psi}_i(\mathbf{r}) \frac{\partial \tilde{\psi}_i^*(\mathbf{r})}{\partial R_I} + \epsilon_i \tilde{\psi}_i^*(\mathbf{r}) \frac{\partial \tilde{\psi}_i^*(\mathbf{r})}{\partial R_I} \right\} = \frac{\partial E_o}{\partial R_I}\bigg|_{\{\tilde{\psi}_i\}} + \sum_i \epsilon_i \frac{\partial}{\partial R_I} \langle \tilde{\psi}_i | \tilde{\psi}_i \rangle \quad (2.23)$$

However, since $\{\psi_i\}$ are normalized, the second term in the last equation disappears. In fact, if we recall that the solutions $\{\psi_i\}$ are those wave functions that minimize the total energy functional, then it is natural that the first derivative of E_0 with respect to ψ_i yields zero. Finally, we have a simple expression for the force on ions:

$$F_I = -\frac{\partial E_o}{\partial R_I}\bigg|_{\{\tilde{\psi}_i\}} - \frac{\partial E_{ii}}{\partial R_I} = -\int d\mathbf{r}\, n_o(\mathbf{r}) \frac{\partial V_{ion}}{\partial R_I} - \frac{\partial E_{ii}}{\partial R_I} \tag{2.24}$$

Eq.(2.24) is called Hellman-Feynman theorem [64].

2.1.6 Plane wave basis and Pseudo-potential

Once the Kohn-Sham equations are subject to periodic boundary conditions, we can identify the quantum i to be $n\mathbf{k}$ where n is the band index and $\mathbf{k}$ is the crystal momentum. The equations now explicitly read:

$$\left(-\frac{\hbar}{2m}\nabla^2 + V_{KS}\right)\psi_{n\mathbf{k}}(\mathbf{r}) = \epsilon_{n\mathbf{k}}\psi_{n\mathbf{k}}(\mathbf{r}) \tag{2.25}$$

Where $$V_{KS}(\mathbf{r}) = V_{ion}(\mathbf{r}) + \int d\mathbf{r}' \frac{n(\mathbf{r}')}{|\mathbf{r}-\mathbf{r}'|} + V_{xc}(\mathbf{r}) \tag{2.26}$$

And $$n(\mathbf{r}) = \sum_{n\mathbf{k}} |\psi_{n\mathbf{k}}(\mathbf{r})|^2 \tag{2.27}$$

Given an explicit V_{KS}, we now have the practical issue on how to solve these coupled equations (Eq. (2.25) and Eq. (2.27)) efficiently.

2.1.6.1 Plane wave basis

To solve the Kohn-Sham equations numerically, we need to choose a basis to expand the wave functions ψ_{nk} and then truncate the basis to make the simulation time finite. The

most natural choice of basis is plane waves because the Bloch states ψ_{nk} have a periodic part which can be expanded in Fourier series.

$$\psi_{n\mathbf{k}}(\mathbf{r}) = e^{i\mathbf{k}.\mathbf{r}} u_{n\mathbf{k}}(\mathbf{r}) = e^{i\mathbf{k}.\mathbf{r}} \sum_{\mathbf{G}} c_{n\mathbf{k}}(\mathbf{G}) \frac{e^{i\mathbf{G}.\mathbf{r}}}{\sqrt{\Omega}} \tag{2.28}$$

Where Ω = the volume of the unit cell.

Insert Eq. (2.28) into the Kohn-Sham equations Eq. (2.25) to find that c_{nk}(G) satisfy:

$$\frac{|\mathbf{k}+\mathbf{G}|^2}{2} c_{n\mathbf{k}}(\mathbf{G}) + \sum_{\mathbf{G}'} \tilde{V}_{KS}(\mathbf{G}-\mathbf{G}') c_{n\mathbf{k}}(\mathbf{G}') = \epsilon_{n\mathbf{k}} c_{n\mathbf{k}}(\mathbf{G}) \tag{2.29}$$

Where $\tilde{V}_{KS}$ is the Fourier transform of V_{KS}. We need to set up a cutoff to get finite number of {G} basis:

$$\frac{|\mathbf{k}+\mathbf{G}|^2}{2} \le E_{cut} \tag{2.30}$$

By Eq. (2.29) and Eq. (2.30), though in principle any accuracy can be achieved by increasing E_{cut}, in practice this method does not work. This occurs because the core electrons in molecules are tightly bound to the nuclei and their wave functions change rapidly in the core region and decay away swiftly. In order to accurately describe those wave functions, we need many plane waves to expand those functions. However, on the other side, those core electrons are so tightly bound to the nuclei that they participate little in the bonding of solids or molecules. So, by using only plane wave basis there is huge calculation associated to describe those electrons that do not play important roles in the properties which we are interested in.

2.1.6.2 Pseudo-potentials

As explained in the previous section, the bonding properties of materials largely depend on valence electrons rather than core electrons. Core electrons having treated immobile

are removed from the computation. However, numerical calculations involving wave functions of valence electrons are huge due to the need of excess plane wave basis for describing rapid oscillation of wave functions in the core region created by valence electrons.

In order to solve this problem, an artificial potential that accurately reproduces the wave functions of valence electrons in the interstitial region and eliminates the oscillating part of wave functions is constructed. This idea is formalized into the so-called pseudo-potentials [75],[76]. Numerous tests show that implementation of pseudo-potential in realistic simulations not only significantly reduces computation cost but also furnishes good description of chemical bonding. Once the pseudo-potential is obtained, the implementation into the Kohn-Sham equations is straightforward. In Eq. (2.09) and Eq. (2.10), the local ionic potential $V_{ion}(\mathrm{r})$ is replaced by a pseudo-potential $V_{ps}(\mathrm{r})$, and every other term remains the same.

2.2 Non-Equilibrium Green's Functions (NEGF)

Non-Equilibrium Green's Function (NEGF) [67]-[79] is used for simulating transport properties of ballistic transistors. A top gate ballistic transistor has left electrode, central region and right electrode. The methods of how NEGF is applied in the device to solve transport phenomena are discussed below.

2.2.1 Non-Equilibrium Electron Distribution

In a transistor the left and right electrodes are assumed equilibrium systems with periodic boundary conditions and the properties of these systems are obtained using a

conventional electronic structure calculation. The challenge in calculating the properties of a device system lies in the calculation of the non-equilibrium electron distribution in the central region.

The assumption is that the system is in a steady state such that the electron density of the central region is constant in time. The electron density is given by the occupied Eigen states of the system. Since the chemical potential is different in the two electrodes, the contribution from each electrode reservoir must be calculated independently.

$$n(\mathbf{r}) = n^L(\mathbf{r}) + n^R(\mathbf{r}) \tag{2.31}$$

The electron contribution from the left, n^L, and right electrode, n^R, can be obtained by calculating the scattering states, which are the Eigen state with scattering boundary conditions. The left and right density are now calculated by summing up the occupied scattering states,

$$n^L(\mathbf{r}) = \sum_\alpha |\psi_\alpha(\mathbf{r})|^2 f(\frac{\varepsilon_\alpha - \mu_L}{kT}) \tag{2.32}$$

$$n^R(\mathbf{r}) = \sum_\alpha |\psi_\alpha(\mathbf{r})|^2 f(\frac{\varepsilon_\alpha - \mu_R}{kT}) \tag{2.33}$$

The scattering states of the system are calculated by first calculating the Bloch states in the electrodes and subsequently solving the Schrödinger equation of the central region using the Bloch states as matching boundary conditions.

2.2.2 Electron Density Matrix

The electron density is given in terms of the electron density matrix. We divide the density matrix into left and right contributions,

$$D = D^L + D^R \qquad (2.34)$$

The left density matrix contribution is now given from NEGF theory by [67]

$$D^L = \int \rho^L(\varepsilon) f(\frac{\varepsilon - \mu_L}{k_B T_L}) d\varepsilon \qquad (2.35)$$

Where

$$\rho^L(\varepsilon) \equiv \frac{1}{2\pi} G(\varepsilon) \Gamma^L(\varepsilon) G^\dagger(\varepsilon) \qquad (2.36)$$

is the spectral density matrix. Note that while there is a non-equilibrium electron distribution in the central region, the electron distribution in the electrode is described by a Fermi function f with an electron temperature T_L.

Furthermore in this equation, G is the retarded Green's function, and

$$\Gamma^L = \frac{1}{i}(\sum^L - (\sum^L)^\dagger) \qquad (2.37)$$

is the broadening function of the left electrode, given in terms of the left electrode Self Energy $\sum^L$. A similar equation exists for the right density matrix contribution.

2.2.3 Retarded Green's Function

The key quantity to calculate is the retarded Green's function matrix,

$$G(\varepsilon) = \frac{1}{(\varepsilon + i\delta_+)S - H} \qquad (2.38)$$

Where δ_+ is an infinitesimal positive number.

S and H are the overlap and Hamiltonian matrices, respectively, of the entire system.

The Green's function is only required for the central region and can be calculated from the Hamiltonian of the central region by adding the electrode Self Energies

$$G(\varepsilon) = [(\varepsilon + i\delta_+)S - H - \sum^L(\varepsilon) - \sum^R(\varepsilon)]^{-1} \quad (2.39)$$

In this work the matrix is stored in a sparse format, and the inversion is done using an O(N)algorithm [80].Self Energy is calculated by iterative Krylov subspace method proposed by H.H. Sørensen *et al.* [81]-[82].

2.2.4 Spill-in Terms

In terms of the density matrix, D, the electron density of the central region is given by

$$n(\mathbf{r}) = \sum_{ij} D_{ij}\phi_i(\mathbf{r})\phi_j(\mathbf{r}) \quad (2.40)$$

The Green's function of the central region gives the density matrix of the central region, D_{CC}, however, to calculate the density correctly close to the central cell boundaries the terms involving, $D_{LL,}$ $D_{LC,}$ $D_{CR,}$ D_{RR} are also needed. These terms are denoted spill-in terms.

In this work all the spill-in terms are included, both for calculating the electron density n(r) and the Hamiltonian integral. This gives additional stability and well-behaved convergence in the device algorithm.

2.2.5 Effective Potential

Once the non-equilibrium density is obtained the next step in the self-consistent calculation is the calculation of the effective potential. The calculation of the exchange-

correlation potential is straight forward since it is a local or semi-local function of the density. However, the calculation of the electrostatic Hartree potential requires some additional consideration in the device system.

The starting point is the calculation of the self-consistent Hartree potential in the left and right electrodes. The Hartree potential of a bulk system has an arbitrary zero, however, the Hartree potentials of the two electrodes can be aligned through their chemical potentials (i.e. Fermi levels), since these are related by the applied bias

$$\mu_R - \mu_L = eV_b \tag{2.41}$$

The Hartree potential of the central region is now obtained by solving the Poisson equation, using the bulk-like Hartree potentials of the electrodes as boundary conditions on the interfaces between the electrodes and the central region.

2.2.6 Transmission Co-efficient

When the self-consistent non-equilibrium density matrix has been obtained, it is possible to calculate various transport properties of the system. One of the most notable is the transmission spectrum from which current and differential conductance can be obtained.

The transmission coefficient may also be obtained from the retarded Green's function using

$$T(\varepsilon) = G(\varepsilon)\Gamma^{L}(\varepsilon)G^{\dagger}(\varepsilon)\Gamma^{R}(\epsilon) \tag{2.42}$$

Where

$G(\varepsilon)$= Retarded Green’s Function

$\Gamma(\varepsilon)$= Broadening Function

In NEGF method, transmission co-efficient is the final outcome which can be further manipulated to produce current voltage characteristics of a electronic device. The method of determining current voltage characteristics from transmission spectrum is discussed in Chapter 3. The peaks in the transmission spectrum predict the probability of the participation of Eigen channels in transport through the channel.

Chapter 3

Model and Computational Details

In this chapter the structure of graphene/hexagonal boron nitride bilayer system and detailed computational methods are discussed. Moreover, methodologies for determining various electronic parameters are also discussed in brief.

3.1 Graphene/ Hexagonal Boron Nitride Bilayer System

Graphene/ Hexagonal Boron Nitride (C/h-BN) bilayer system has three variants [63]:

1. B1 Configuration: where one C atom is directly above the B atom and other C atom above the center of h-BN
2. B2 Configuration: where one C atom is directly above N atom and other C atom above the center of h-BN
3. B3 Configuration: where one C atom is directly above the B atom and the other C atom directly above N

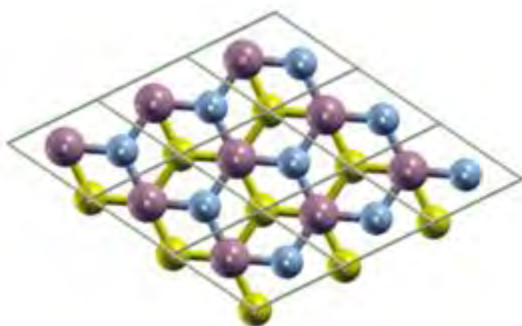

Figure 3.1(a): B1 Top

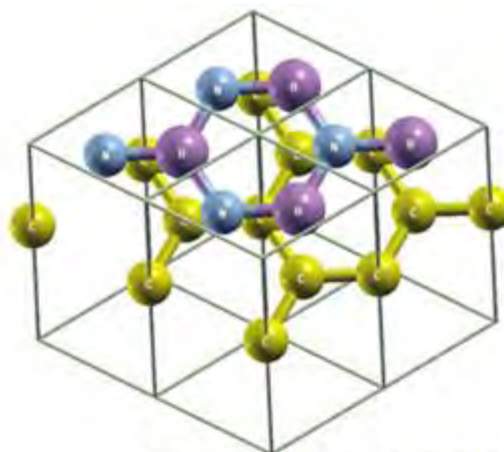

Figure 3.1 (b): B1 upside

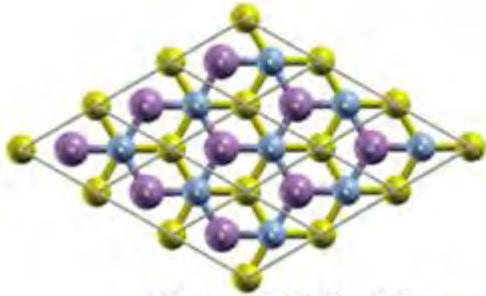

Figure 3.2 (a): B2 top

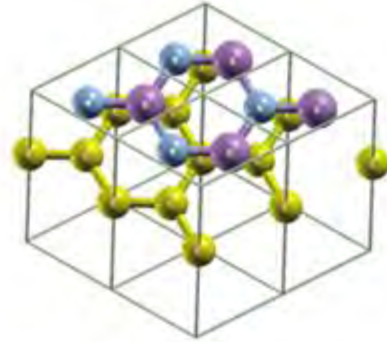

Figure 3.2 (b): B2 upside

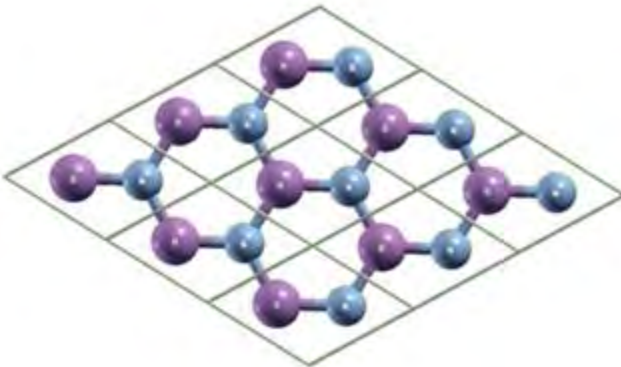

Figure 3.3 (a): B3 top

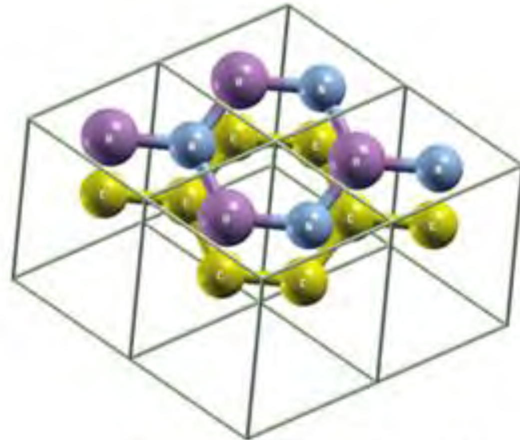

Figure 3.3 (b): B3 upside

3.2 Computational Details

The electronic properties of the proposed super lattice are investigated using density-functional theory (DFT) with a plane-wave basis set. Perdew-Zunger variant LDA (Local Density Approximation) was performed using the Ab initio code PWSCF package of Quantum Espresso [65]. To include the electron-ion interaction we have used norm conservative pseudo potentials for all the atoms.

Our calculation methodology started with structural optimization of the B1,B2 and B3 super lattice structure and then a precise self consistent field (SCF) analysis was done to determine the band structure of the super lattice. For the structural optimization the plane wave basis cut off was set at 45 Ry and the convergence threshold on force was 10^{-3} Ry/a.u. A 36×36×1 Monkhorst-Pack k-point grid was used. To avoid the interaction

between repeating unit cells a large vacuum space of 20 Å thickness was maintained throughout the optimization process. Then the lattice parameters were varied for different interlayer distances to determine the optimum unit cell for the structures.

In the next part of SCF calculation a 36×36×1 k-points Monkhorst-Pack grid was employed for better accuracy. The convergence threshold for self consistency in energy was set at 10^{-8} Ry. All atomic position and unit cell parameters found as the final output of geometry optimization and relaxation process were used for SCF and band-structure calculation. The band structure is plotted on the lines joining the high-symmetry points Γ, M, K and Γ.

3.3 Methodology

In this section methods for determining various electronic parameters are discussed.

3.3.1 Effective Mass

The formula for calculating carrier effective mass used in our work:

$$m^* = \frac{^2}{\partial^2 E / \partial k^2} \quad (3.1)$$

The second derivative was evaluated on the lowest conduction band minima using five point stencil method [83], [84].The energy dispersion near the lowest conduction band minima is almost linear like graphene. For longitudinal effective mass Γ to K path was considered. For transverse effective mass the direction perpendicular to Γ to K path was considered.

Previous works [63], [85] have exploited this linearity to extract the electron effective mass using the formula

$$m^* \cong \frac{E_g}{2^* v_f^2} \quad (3.2)$$

Where, E_g is the band gap and v_f is the Fermi velocity. But here we have tried to consider the meagre non-linearity present in the conduction band minima region and evaluate the effective mass using Eq. (3.1) and found that this is in good agreement with the works based on Eq. (3.2).

3.3.2 Fermi Velocity

The electron Fermi velocity is calculated by fitting a straight line through the lowest conduction band minima and nearby almost linear points and then its slope was determined to calculate the group velocity using the equation:

$$v_g = \frac{\partial E}{\partial k} \quad (3.3)$$

Similarly, the hole Fermi velocity is calculated by fitting a straight line through the highest valence band maxima and nearby almost linear points and then its slope was determined to calculate the group velocity using the same equation.

3.3.3 IV Characteristics

The current is calculated from the transmission coefficient (the method for deriving transmission coefficient is discussed in Chapter 2) using:

$$I(V_L, V_R, T_L, T_R) = \frac{e}{h}\sum_\sigma \int T_\sigma(E)\left[f\left(\frac{E-\mu_R}{k_B T_R}\right) - f\left(\frac{E-\mu_L}{k_B T_L}\right)\right] dE \quad (3.4)$$

where f is the Fermi function, $T_{L/R}$ is the electron temperatures of the left/right electrode, and $T_\sigma (E)$ is the transmission coefficient for the spin component σ

The chemical potentials of the left electrode $\mu_L = E_F^L - eV_L$; and the right electrode, $\mu_R = E_F^L - eV_R$ are defined relative to the Fermi level of the left electrode, and related to the applied bias through

$$\mu_R - \mu_L = eV_{bias} \quad (3.5)$$

$$V_{bias} = V_L - V_R \quad (3.6)$$

Positive current flows when the applied voltage for the left electrode is higher than that of the right one, thus the positive current direction is left to right. A positive current corresponds to the flow of charge from left to right, meaning that the flow of electrons is right-to-left, (since electrons have a negative charge).

3.3.4 Model Validation

At first the B1 structure was reviewed using PWSCF to compare the simulated results with the reported results published by Behera *et al.* [63] to emphasize the accuracy and validity of our calculation. These results are summarized in Table 1 and Fig. 3.4 and Fig. 3.5. While Table 1 illustrates the optimized parameters obtained from both this work and Ref [63], Fig. 3.4 and Fig. 3.5 shows respectively the dependence of band gap and longitudinal electron effective mass on percentage of biaxial strain applied to the super lattice.

Table-3.1: Lattice Parameter and band gap for B1

	Simulated Result	**Reported by Behera *et al.* [63]**
Lattice parameter (a = b) (Å)	2.481	2.47
Interlayer Distance (Å)	3.241	3.217
Band gap (meV)	58.6	59

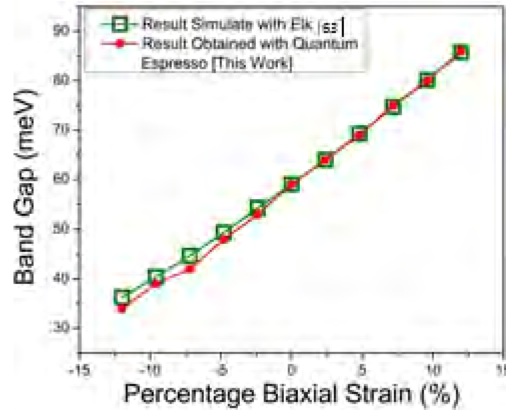

Figure 3.4: The band gap of B1 structure as a function of biaxial strain applied to the super lattice. The red line shows the results obtained in this work and the green line is obtained from the result published by Behera *et al.*[63]

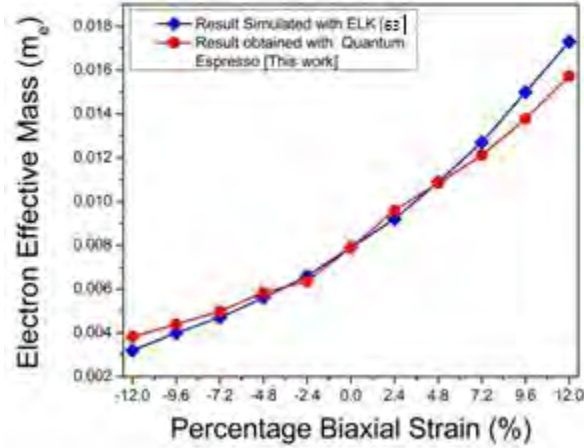

Figure 3.5: Longitudinal electron effective mass of B1 structure as a function of biaxial strain. Result published by Behera *et al.* [63] using Eq. (3.2) is shown in blue line. Electron effective mass calculated using Eq. (3.1) in this work is shown in red line.

Moreover, in this work, the Fermi velocity for optimized B1 structure was found to be 0.855×10^6 m/s, closely matched with 0.8×10^6 m/s reported by Behera *et al.*[63].All these comparisons show very good agreement with the published results and hence validate the accuracy of the model used in this work.

Chapter 4

Results and Discussion: Material Properties

In this Chapter the simulation results for structural optimization and electronic band structure calculation are discussed. Moreover, the effect of biaxial tensile and compressive strain on electronic band structure and density of states (DOS) are also discussed along with some important electronic parameters such as band gap, carrier effective mass and Fermi velocity.

4.1 Atomic Structure and Geometry Optimization

The optimization process was performed iteratively by varying both interlayer distance and lattice parameter and observing the minima of the potential energy surface. A built in variable cell relaxation function of PWSCF was run to verify the iterative process. The result for B1 configuration is shown in Fig. 4.1, from which it is seen that the lattice parameter of this configuration is 2.48 Å and the inter layer distance is 3.2 Å.

A more precise relaxation process reveals that the optimized lattice parameter is 2.481Å and the interlayer distance is 3.241Å, which agrees with the lattice parameter of 2.47 Å and interlayer distance of 3.217Å reported by Behera *et al.* [63].

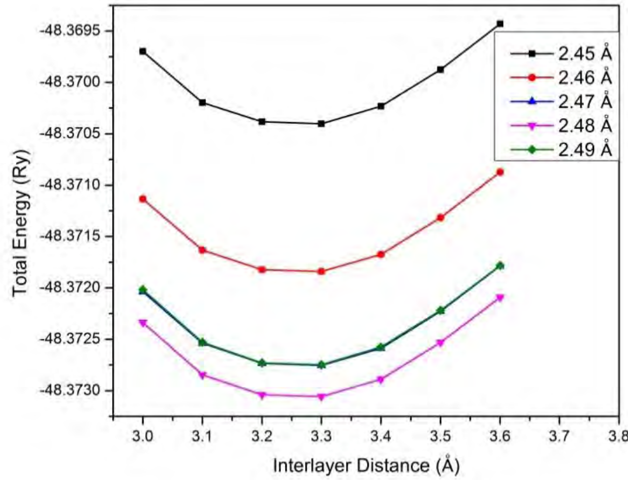

Figure 4.1: The total energy of B1 structure as a function of lattice parameter and interlayer distance.

The results for B2 and B3 configuration are shown in Fig. 4.2 and Fig. 4.3 respectively, from which it is seen that the lattice parameter of both B2 and B3 configuration is 2.48 Ǻ whereas the inter layer distance of B2 and B3 is 3.4 Ǻ and 3.5 Ǻ respectively.

A more precise relaxation process reveals that for B2 the optimized lattice parameter is 2.4805Ǻ and the interlayer distance is 3.44 Ǻ, whereas for B3 the optimized lattice parameter is 2.478Ǻ and the interlayer distance is 3.5675Ǻ. These values are in very good agreement with the reported values of lattice parameter 2.47 Ǻ (For bothB2 and B3) [50] and interlayer distances of 3.4Ǻ (B2) and 3.5Ǻ (B3) [86].

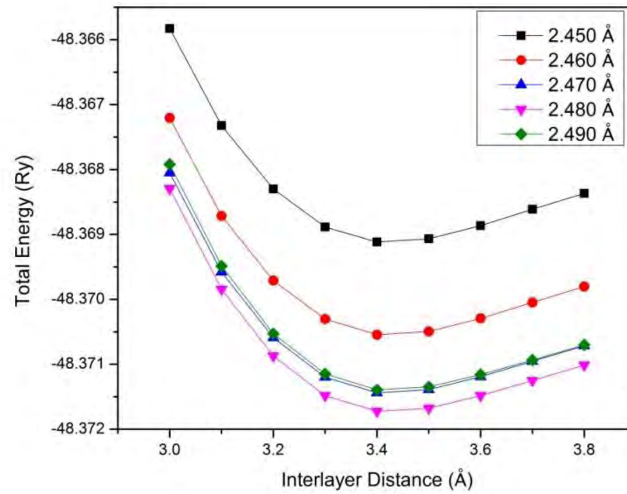

Figure 4.2: The total energy of B2 structure as a function of lattice parameter and interlayer distance.

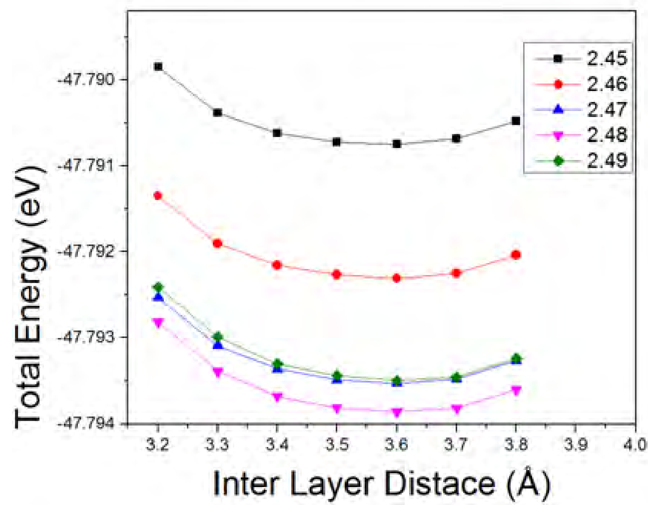

Figure 4.3: The total energy of B3 structure as a function of lattice parameter and interlayer distance.

It is evident from the graphs that B1 has the highest stability and the order of stability is in literature [63].

4.2 Electronic Structure

4.2.1 Band Structure

The band structure of the super lattice was calculated along the line joining the high symmetry points Γ, M, K and Γ in the Brillouine Zone. A total of 903 points was taken along the line using the Xcrysden [87]. Care was taken to calculate the empty bands with the same accuracy as for the filled bands.

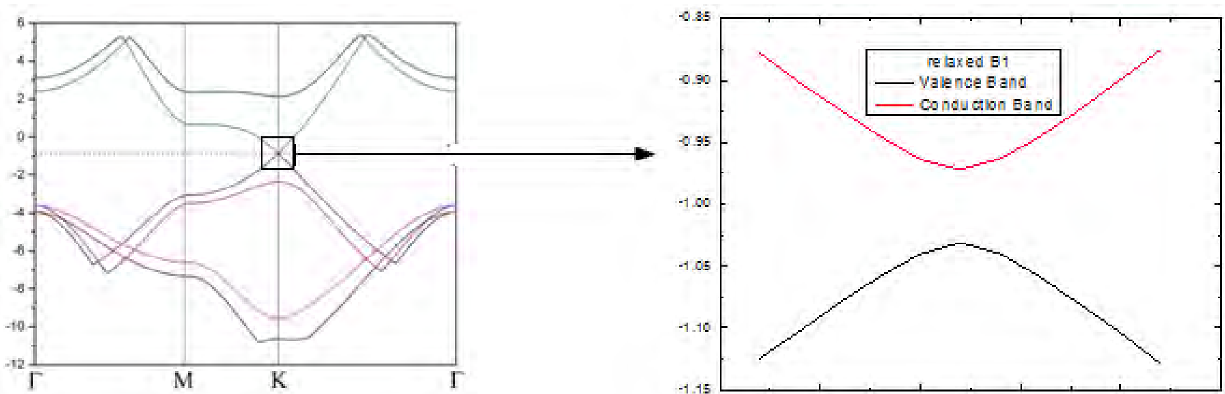

Figure 4.4: Band structure for optimized structure of B1 configuration

The band structure for the optimized and relaxed super lattice of B1 configuration is shown in Fig. 4.4 and a direct band gap of 58.6 meV was obtained for this case. From the zoomed band structure shown in Fig 4.4 it is evident that it preserves almost linear cone like relationship near the Dirac point, a characteristic very similar to pristine graphene and indicates massless Fermion like nature of the carriers. So it is expected for this super lattice to preserve the attractive and promising electronic characteristics of graphene.

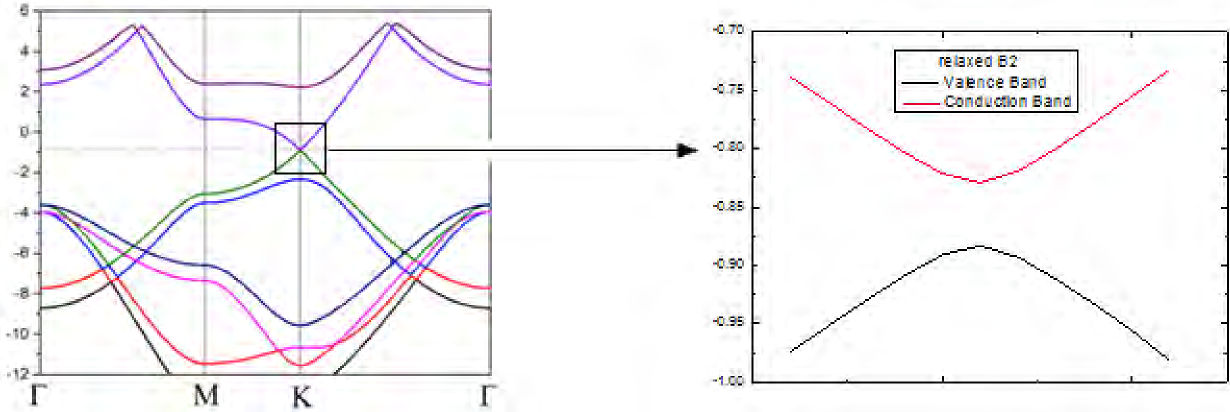

Figure 4.5: Band structure for optimized structure of B2 configuration

The band structure for optimized B2 and B3 is shown in Fig. 4.5 and Fig. 4.6 respectively, from where it is clear that both the configurations show the same trend as B1. So all the configurations of C/h-BN HBL show somehow characteristics similar to graphene and hence the electrons will show behavior similar to Fermion observed in graphene. From Fig. 4.5 and Fig. 4.6 it is clear that B3 configuration has greater band gap than B2 configuration and both conduction band minima and valence band maxima in B3 shows a less curvature than B2.From the band structure the band gap of B2 and B3 is calculated as 54.3meV and 70.4 meV respectively.

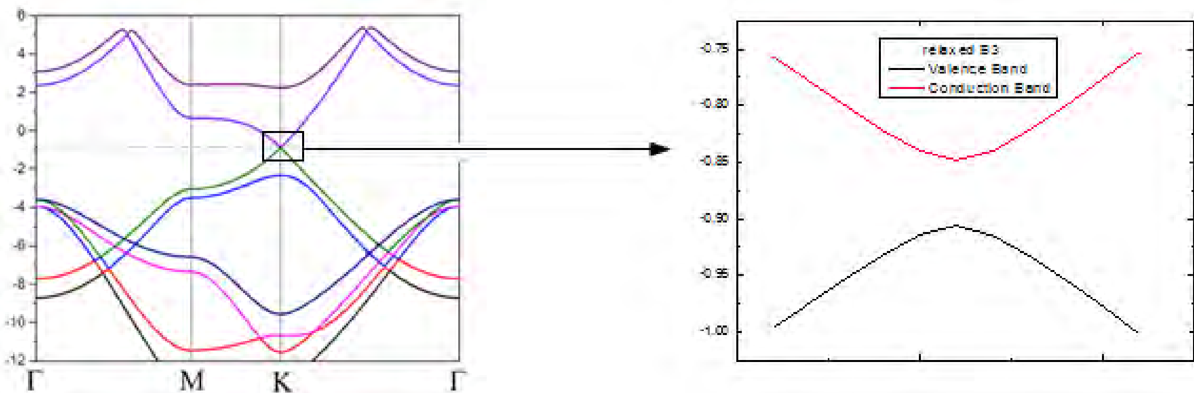

Figure 4.6: Band structure for optimized structure of B3 configuration

4.2.2 Density of states (DOS)

The DOS for B1, B2 and B3 are shown in Fig. 4.7, Fig. 4.8 and Fig. 4.9 respectively, where in (A) the DOS and in (B) the integrated DOS are placed. In two dimensional materials integrated DOS plays significant role in describing electronic properties of material and hence it is produced in this work. Interestingly, the linear shape in integrated DOS of B1, B2 and B3configurations is the same trend observed in graphene. Hence all the configurations of C/h-BN HBL show the same trend like graphene not only in terms of band structure shown in the previous section but also in terms of integrated DOS.

There is shown a gap near Fermi line (dotted vertical line) in Fig. 4.7 (A), 4.8 (A) and Fig. 4.9 (A) which is almost same to the band gap. So, band gap of the configurations can also be derived from the DOS in addition from band structure which is shown in the previous section. The band gap for B1, B2 and B3 calculated from the DOS is 58meV, 54meV and 70meV almost similar to the results obtained from band structure in the previous section.

The peaks in DOS of B1, B2 and B3 are almost similar as the DOS is basically composed of the s and p orbitals of carbon, boron and nitrogen. Almost negligible contribution is from d orbital as the outermost electrons in carbon, boron and nitrogen do not exist in d orbital. Slight change in the gap near Fermi line is observed due to the change in the orientation of atoms in the configurations. It is observed that B3 has the highest and B2 has the lowest gap shown in DOS that is consistent with their band gap.

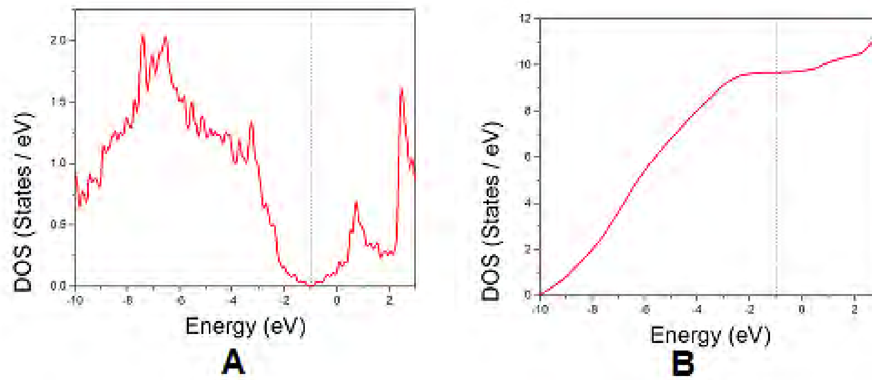

Figure 4.7: DOS for optimized structure of B1: (A) DOS (B) Integrated DOS

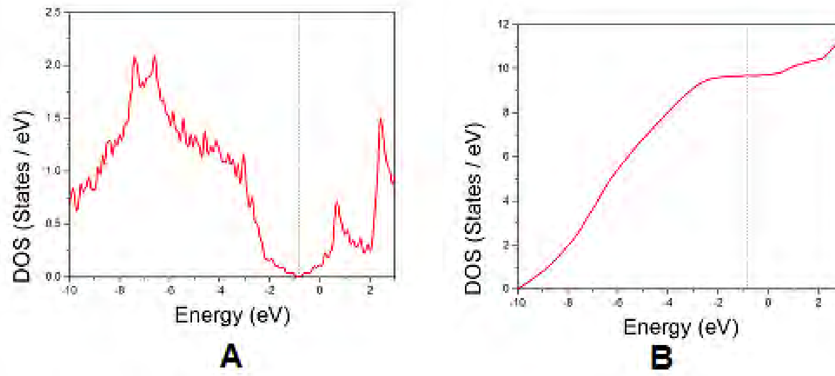

Figure 4.8: DOS for optimized structure of B2: (A) DOS (B) Integrated DOS

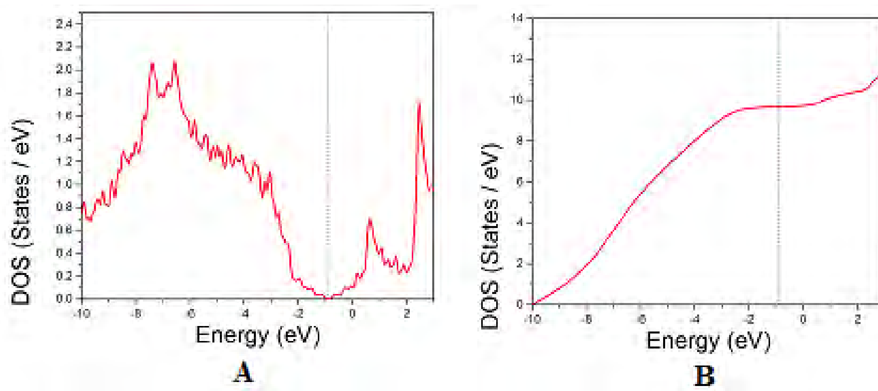

Figure 4.9: DOS for optimized structure of B3 : (A) DOS (B) Integrated DOS

4.3 Effect of Biaxial Strain

After observing the electronic structure of the relaxed configurations, biaxial strain was applied to all the configurations to observe how the electronic structure and hence the material electronic properties vary with strain. Strain was applied by varying the in-plane lattice parameters equally and then relaxing the structure along the direction perpendicular to the plane. Then the DFT under LDA was used to calculate the electronic structure of the configurations of C/h-BN HBL.

4.3.1 Band Structure

First, biaxial strain was applied at the super lattice by varying the lattice parameter. Each time the structure was relaxed before the self-consistent field (SCF) analysis was performed to conduct the band structure determination. The interlayer distance remained almost constant when expanded and slightly increased during compression. The band gap remained direct at the K point and during compression to expansion the band gap increased monotonically. Fig. 4.10, Fig. 4.12 and Fig. 4.13 show all the band structures of the strained super lattice of B1, B2 and B3 respectively.

It is observed in the band structures that the linearity and slope of the bands near K point increase from tensile to compressive strain for all the configurations of C/h-BN HBL. So it will affect the properties of the HBL in terms of Fermi velocity and Fermion like characteristics of the electron. Higher slope means higher Fermi velocity which is very promising for electronic application. By applying compressive strain Fermi velocity is expected to increase, a very significant finding evident from the strained band structures of B1, B2 and B3.

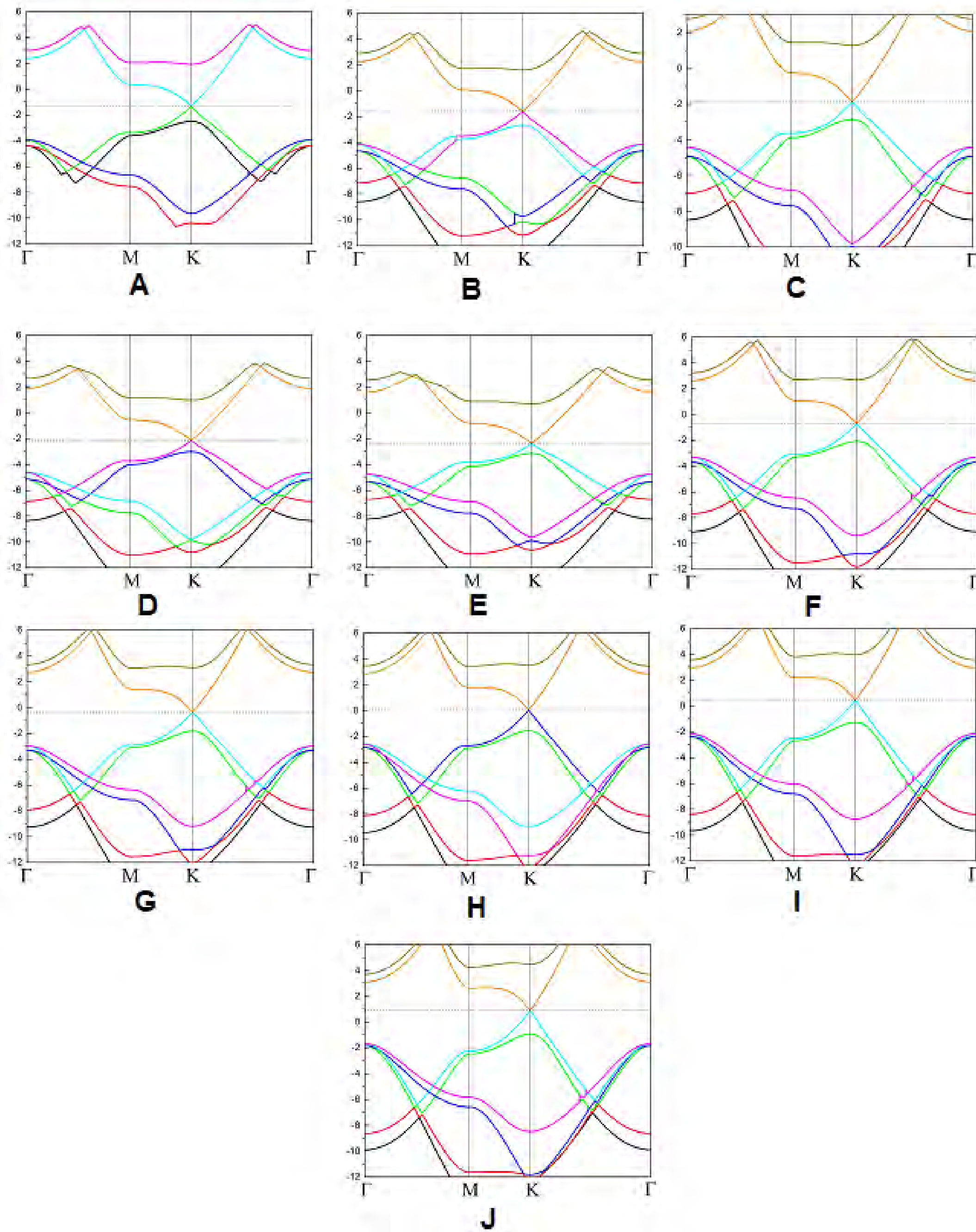

Figure 4.10: The band structures of the strained super lattice (B1 configuration). A to E shows the band structure of super lattice when +2.4%, +4.8%, +7.2%, +9.6% and +12% strain tensile was applied. F to J shows the band structure when the super lattice was compressed to 2.4%, 4.8%, 7.2%, 9.6% and 12% respectively.

The conduction bands and valence bands near high symmetry K point for three strained values of B1 configurations are plotted below in Fig. 4.11 to infer further interpretation from the strained band structure. It is observed that the curvature of both the valence and conduction bands increases from tensile to compressive strain. This curvature is very important in band minima (maxima) to predict the effective mass of electron (hole). The deduction that the slope of the band edges near K point increases from tensile to compressive strain is also substantiated from Fig. 4.11. B2 and B3 also show the same trend as shown in Fig. 4.11 for B1 configuration and hence the results for B2 and B3are not shown here.

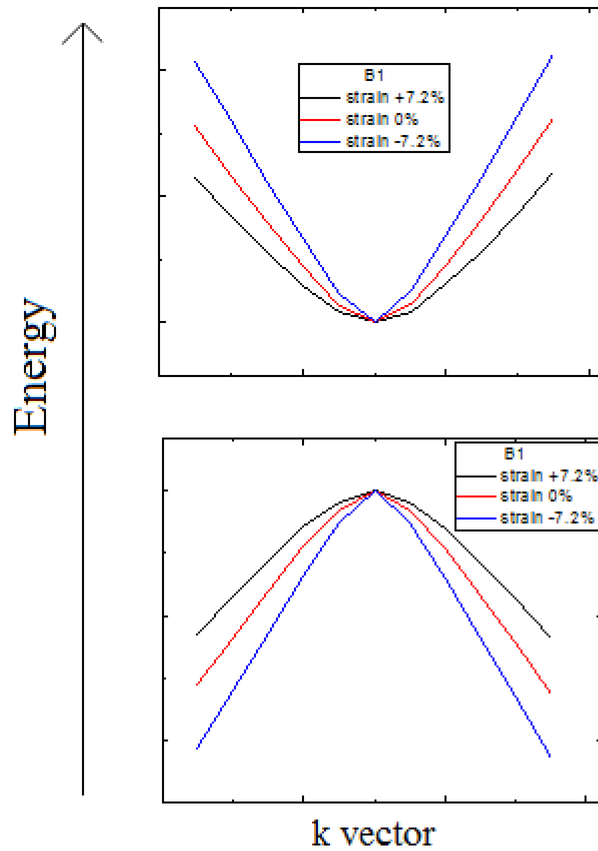

Figure 4.11: Effect of biaxial strain on the band structure of B1 conduction band (top) valence band (bottom)

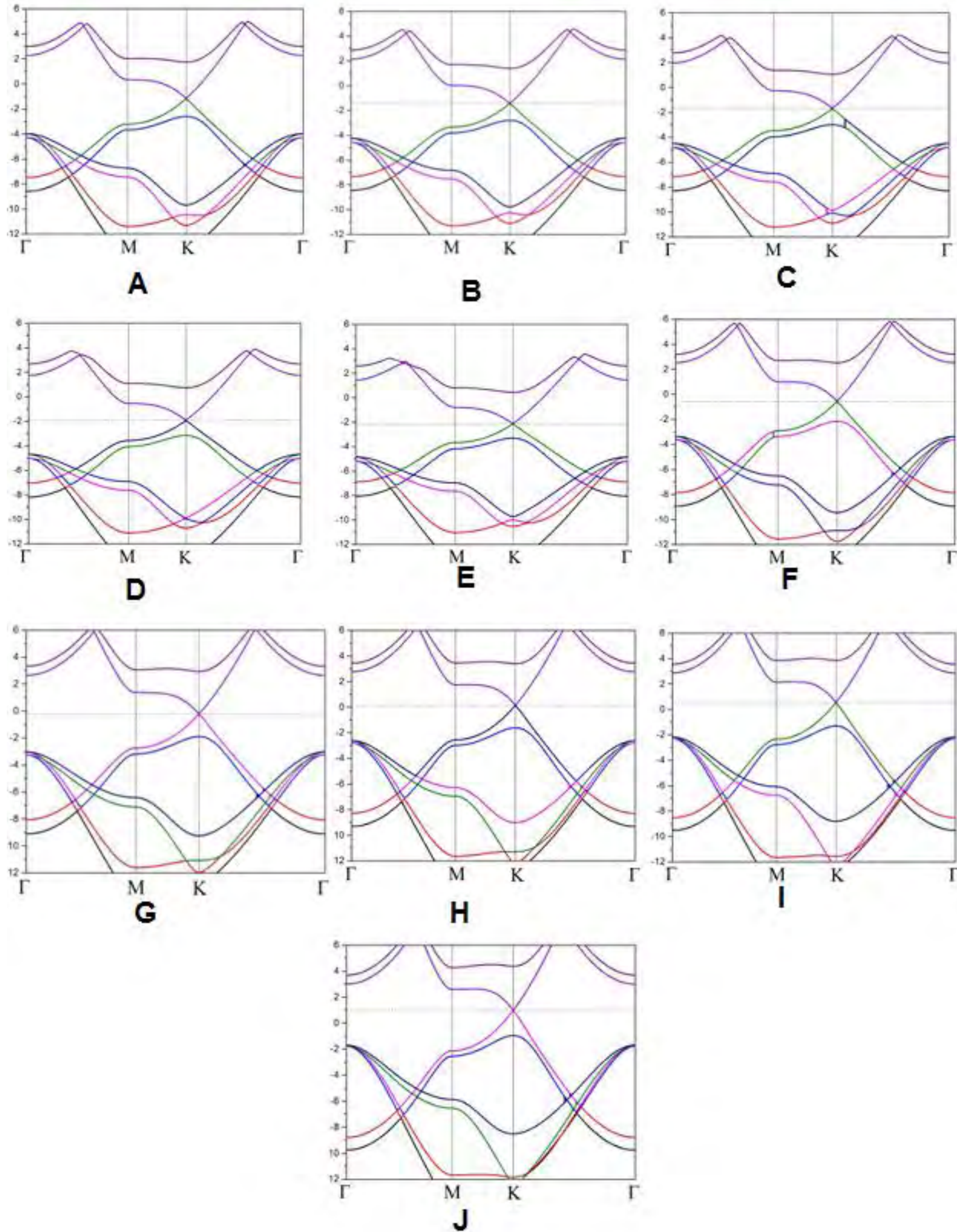

Figure 4.12: The band structures of the strained super lattice (B2 configuration). A to E shows the band structure of super lattice when +2.4%, +4.8%, +7.2%, +9.6% and +12% strain was applied. F to J shows the band structure when the super lattice was compressed to 2.4%, 4.8%, 7.2%, 9.6% and 12% respectively.

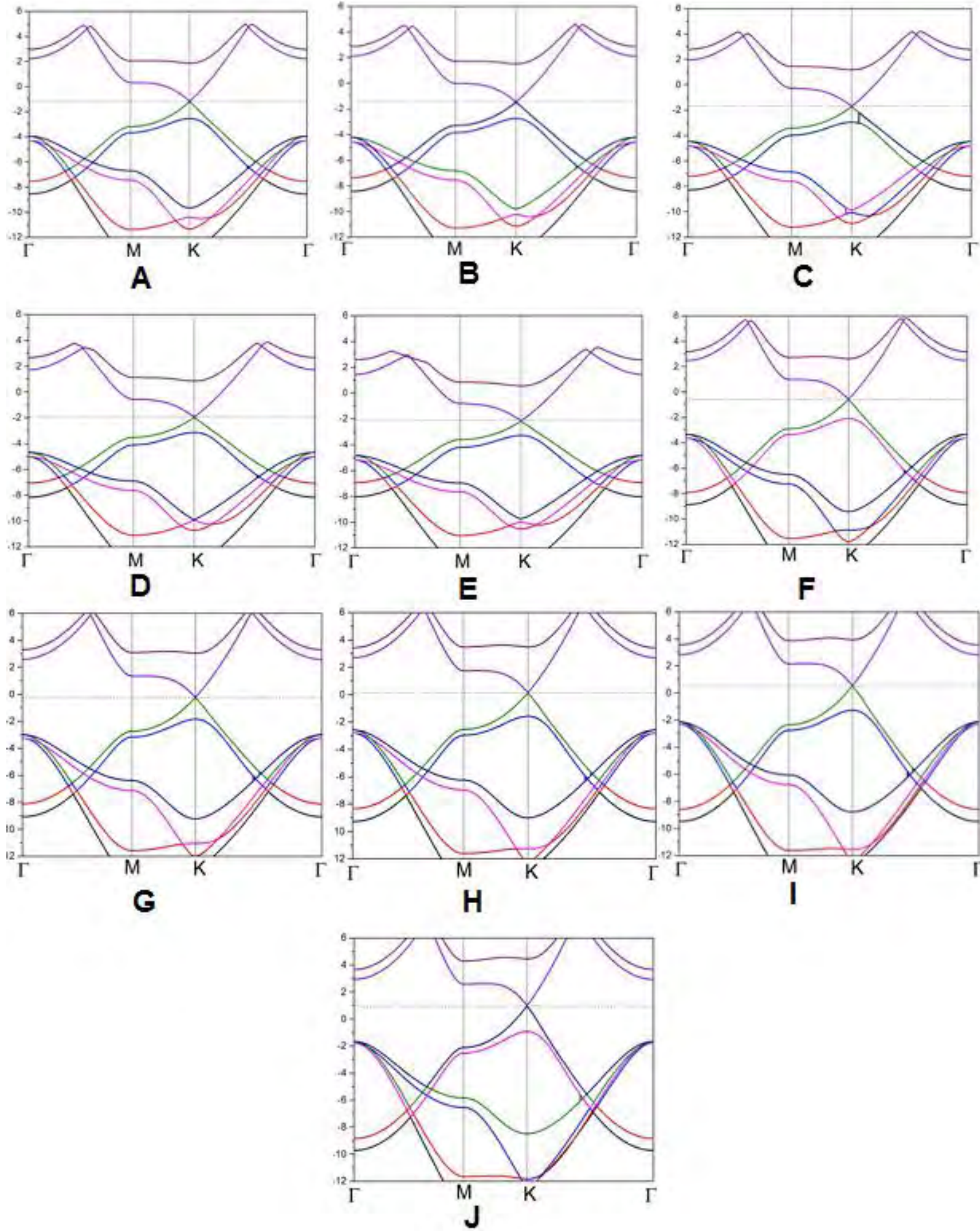

Figure 4.13: The band structures of the strained super lattice (B3 configuration). A to E shows the band structure of super lattice when +2.4%, +4.8%, +7.2%, +9.6% and +12% strain was applied. F to J shows the band structure when the super lattice was compressed to 2.4%, 4.8%, 7.2%, 9.6% and 12% respectively.

4.3.2 DOS

DOS for strained B1, B2 and B3 are shown in Fig. 4.14, Fig. 4.16 and Fig. 4.18 whereas the cumulative DOS is plotted in Fig. 4.15, Fig. 4.17 and Fig. 4.19 respectively. From the DOS it is observed that for higher tensile region the DOS show splits in higher energy domain. This can be explained by the overlapping of orbitals in the higher energy regions for higher tensile strain. For higher compressive value the peak in high energy region is minimized. This can be explained as for the compressive regions the overlap between orbitals is reduced and hence the results are observed in DOS.

From the integrated DOS it is observed that the cumulative value of DOS for compressive strain in high energy regions becomes almost constant and the reduction is created by the reduction of DOS in high energy region discussed in the previous paragraph. For tensile strain it keeps increasing as DOS for tensile strain has high peak value in high energy region just discussed in earlier paragraph. So all the results are in consistent and thus strengthen the validity of this work.

The gap near the Fermi line increases from compressive to tensile strain observed in DOS for all the configurations of C/h-BN HBL. These results are consistent with the discussions in the previous section. The reason was obvious from the band structures as the gap in band structure increased from compressive to tensile strain. The linear shape in low energy region in integrated DOS is very similar to graphene. Hence all the strained structures of C/h-BN HBL preserve the characteristics of graphene which is also a significant finding from this work.

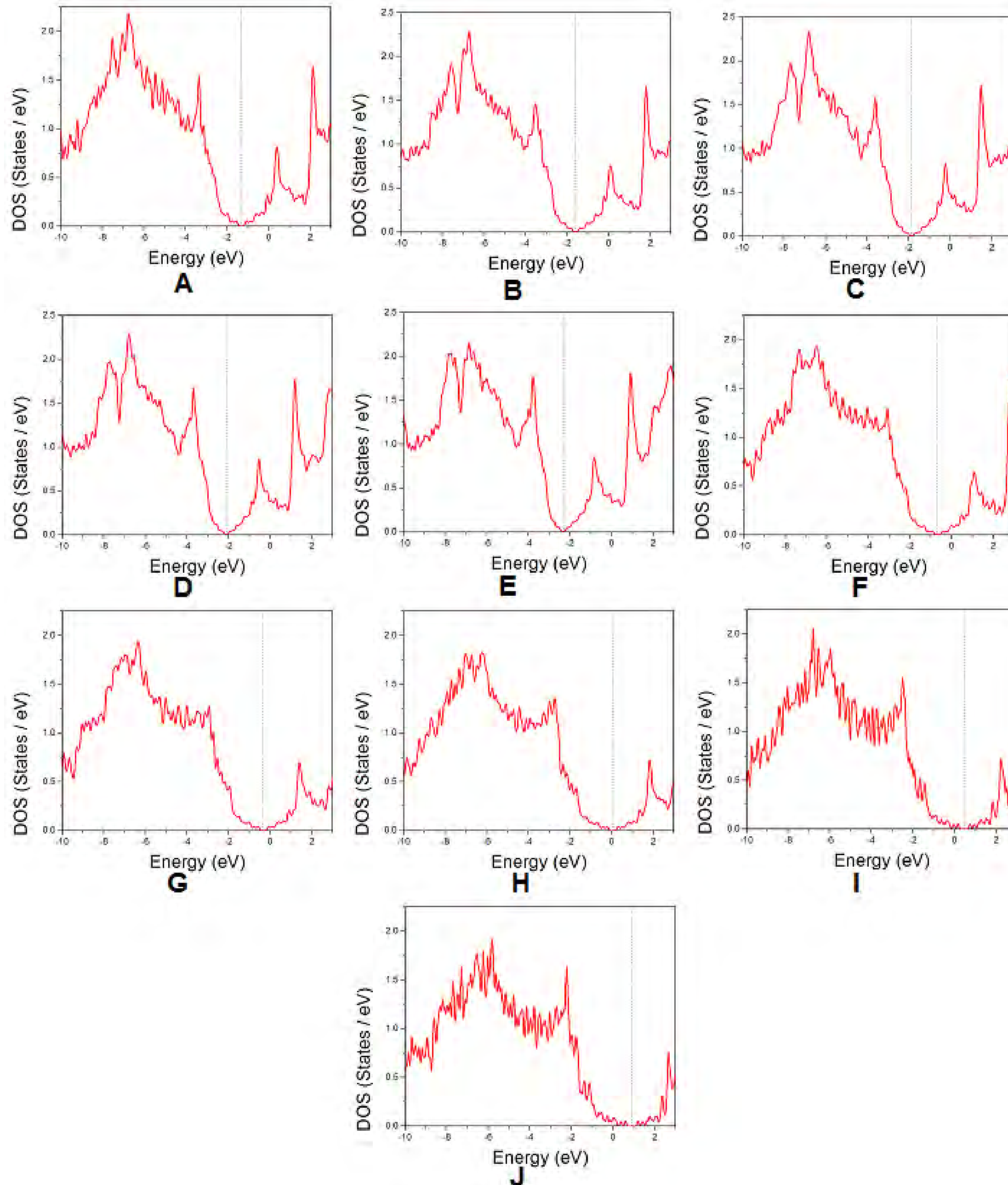

Figure 4.14: The DOS of the strained super lattice (B1 configuration). A to E shows the band structure of super lattice when +2.4%, +4.8%, +7.2%, +9.6% and +12% strain was applied. F to J shows the band structure when the super lattice was compressed to 2.4%, 4.8%, 7.2%, 9.6% and 12% respectively.

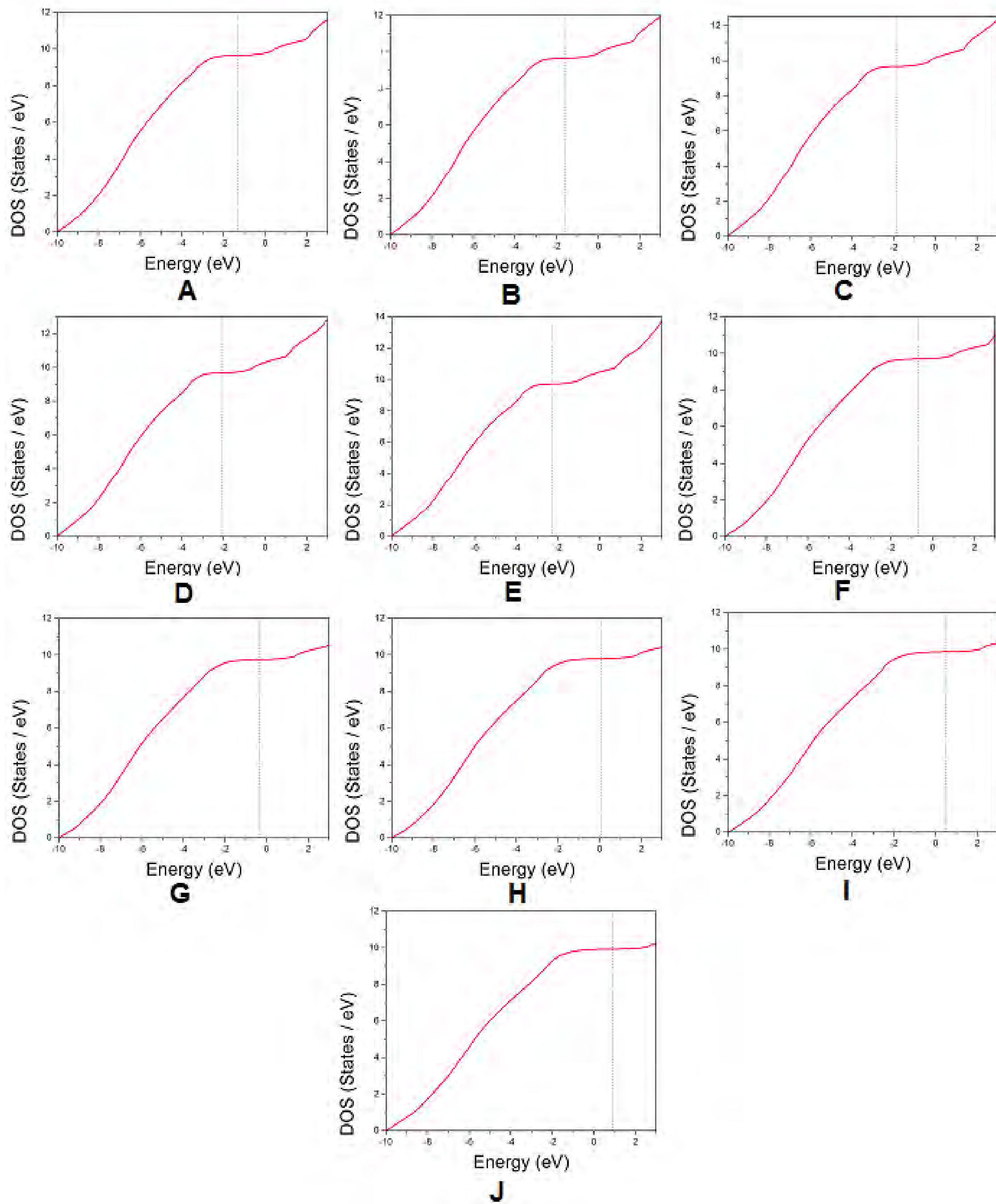

Figure 4.15: The integrated DOS of the strained super lattice (B1 configuration). A to E shows the band structure of super lattice when +2.4%, +4.8%, +7.2%, +9.6% and +12% strain was applied. F to J shows the band structure when the super lattice was compressed to 2.4%, 4.8%, 7.2%, 9.6% and 12% respectively.

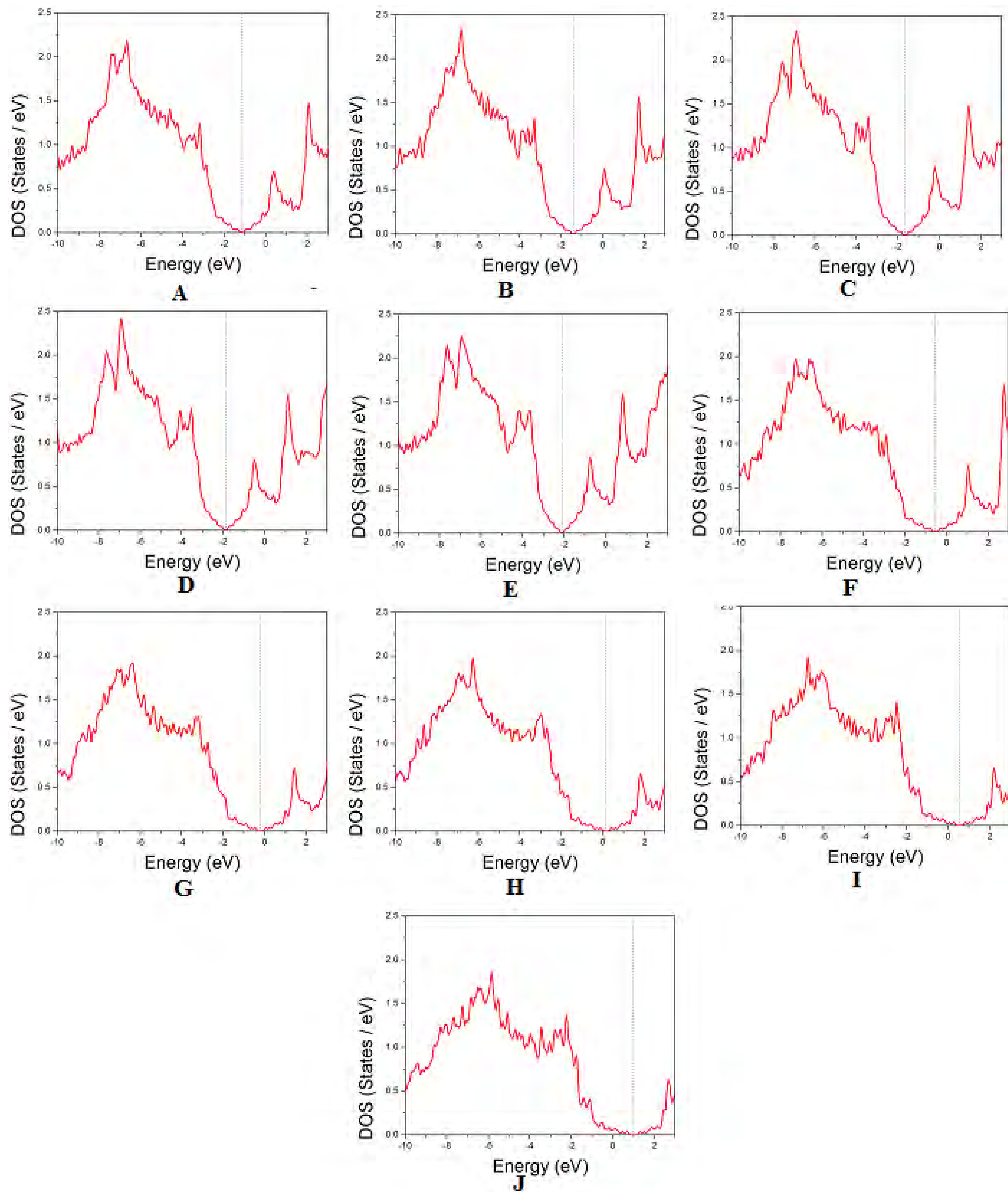

Figure 4.16: The DOS of the strained super lattice (B2 configuration). A to E shows the band structure of super lattice when +2.4%, +4.8%, +7.2%, +9.6% and +12% strain was applied. F to J shows the band structure when the super lattice was compressed to 2.4%, 4.8%, 7.2%, 9.6% and 12% respectively.

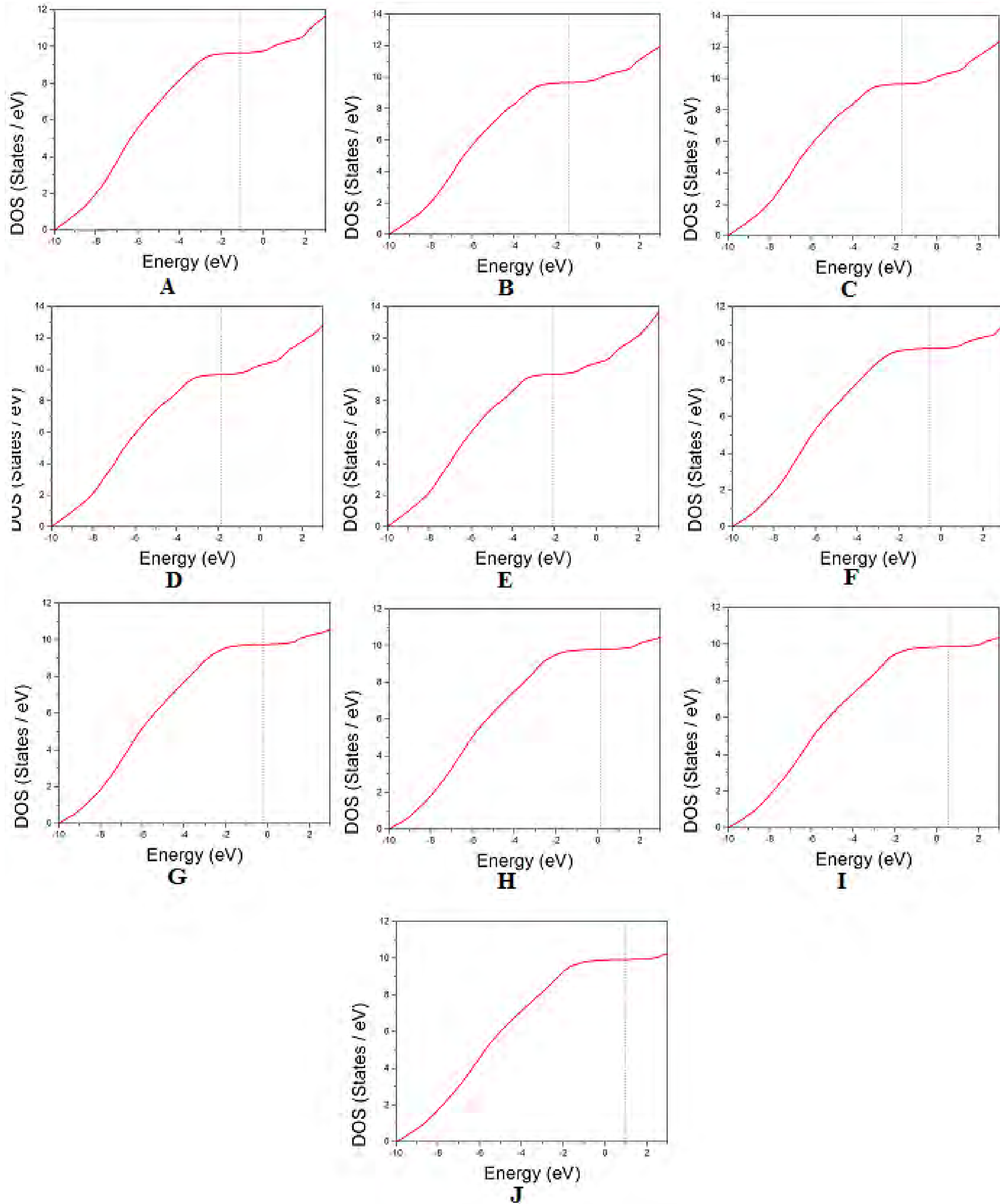

Figure 4.17: The integrated DOS of the strained super lattice (B2 configuration). A to E shows the band structure of super lattice when +2.4%, +4.8%, +7.2%, +9.6% and +12% strain was applied. F to J shows the band structure when the super lattice was compressed to 2.4%, 4.8%, 7.2%, 9.6% and 12% respectively.

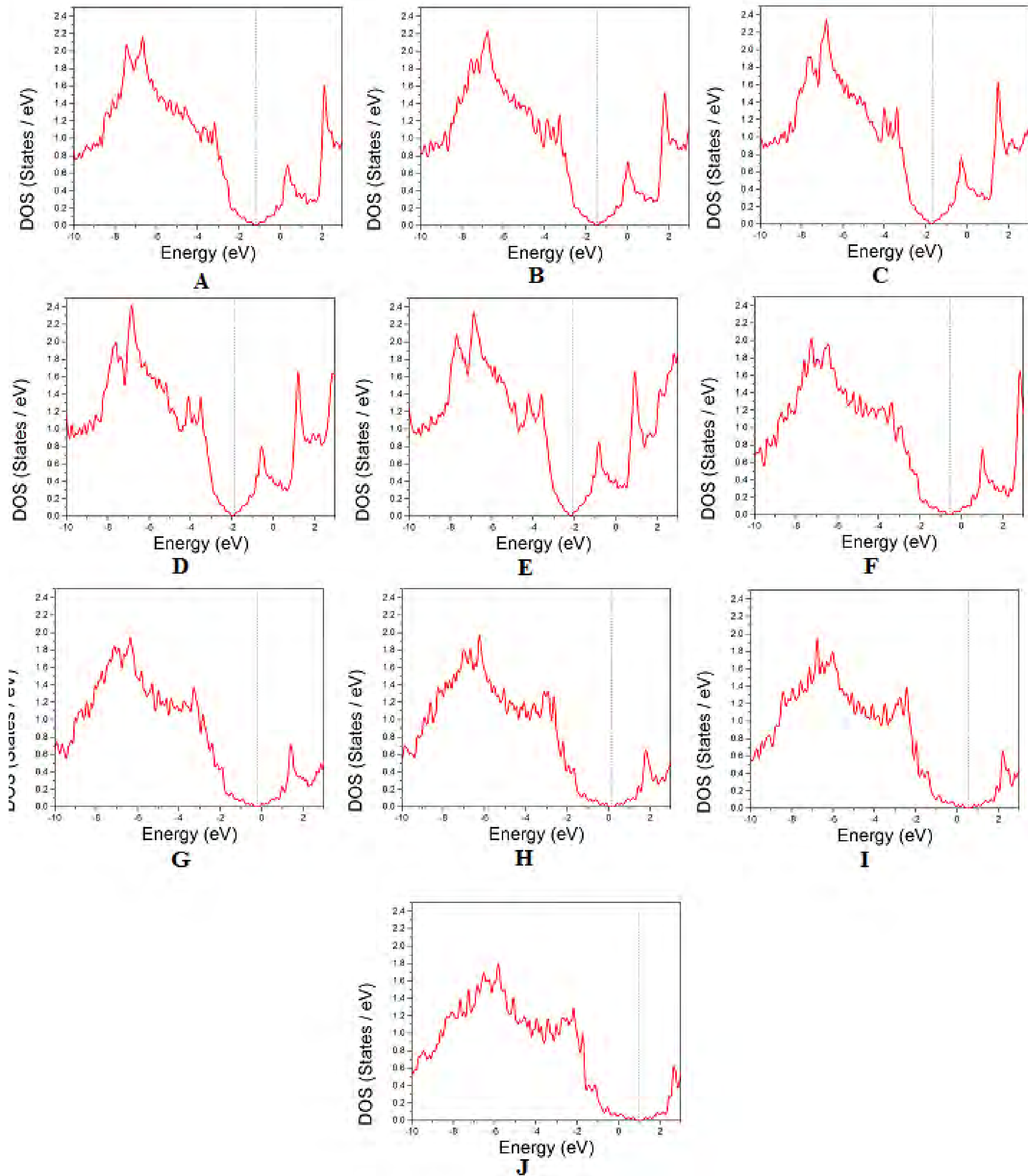

Figure 4.18: The DOS of the strained super lattice (B3 configuration). A to E shows the band structure of super lattice when +2.4%, +4.8%, +7.2%, +9.6% and +12% strain was applied. F to J shows the band structure when the super lattice was compressed to 2.4%, 4.8%, 7.2%, 9.6% and 12% respectively.

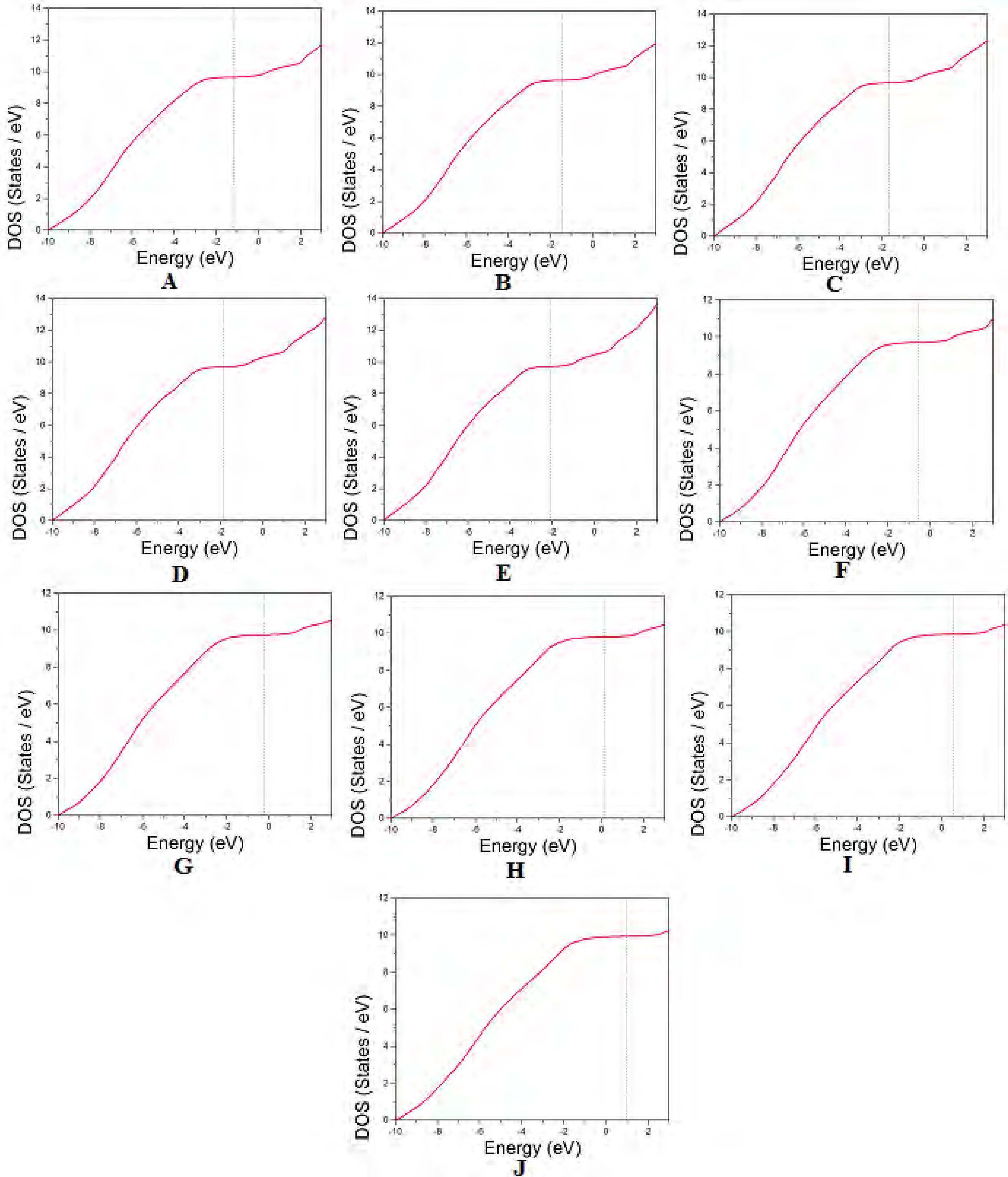

Figure 4.19: The integrated DOS of the strained super lattice (B3 configuration). A to E shows the band structure of super lattice when +2.4%, +4.8%, +7.2%, +9.6% and +12% strain was applied. F to J shows the band structure when the super lattice was compressed to 2.4%, 4.8%, 7.2%, 9.6% and 12% respectively.

4.3.3 Band gap

It is seen from Fig. 4.20 that band gap increases monotonically from compressive to tensile biaxial strain. Band gap of B1 structure is more than B2 structure and B3 has the highest band gap in all the regions except higher compressive area. The calculated band gap of relaxed B1, B2 and B3 are 58.6 meV, 54.3 meV and 70.4 meV respectively.

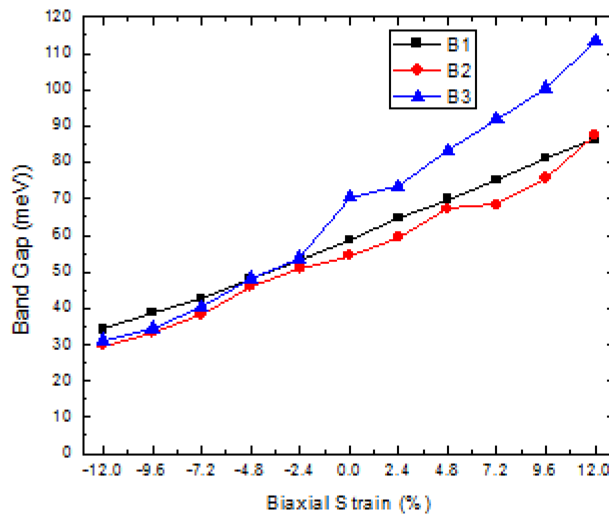

Figure 4.20: The band gap of B1, B2 and B3 as a function of percentage biaxial strain applied to the super lattice.

The reason for difference in band gap among B1, B2 and B3 can be explained from the band structures shown in Fig. 4.4, Fig. 4.5 and Fig. 4.6. It is seen that the gap is highest for B3 and lowest for B2. Moreover, the increase of band gap with tensile strain can be explained as that with tensile strain applied to the structure, it is expanded and the reciprocal lattice structure is decreased. Hence the gap increases in k-space, thus creating greater band gap in tensile strain region.

4.3.4 Effective Mass

4.3.4.1 Electron Effective Mass

Fig. 4.21 indicates that the effective mass of the B1, B2 and B3 structure is almost same except for tensile strain regions. At tensile regions B3 structure shows a rapid increase compared to B1 and B2 structure. The transverse electron effective mass also shows similar trend as longitudinal one which is shown in Fig 4.22.

The reason behind the results can be explained from Fig. 4.11. It is seen that the curvature of all conduction band minima increases with compressive strain. The effective mass of electron is inversely proportional to the curvature of the band near band minima. Hence higher curvature creates lower effective mass (both longitudinal and transverse) for all the configurations of C/h-BN HBL. Here longitudinal effective mass means the mass in Γ to K direction and the transverse effective mass is taken in the direction perpendicular to the Γ to K in k-space.

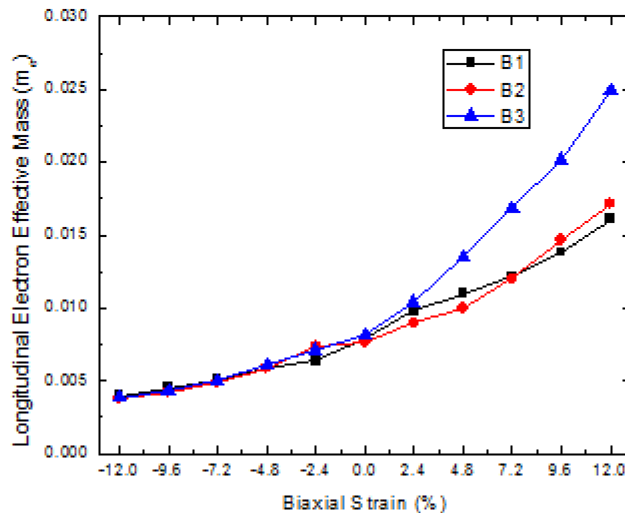

Figure 4.21: Longitudinal electron effective mass of B1, B2 and B3 as a function of percentage biaxial strain applied to the super lattice.

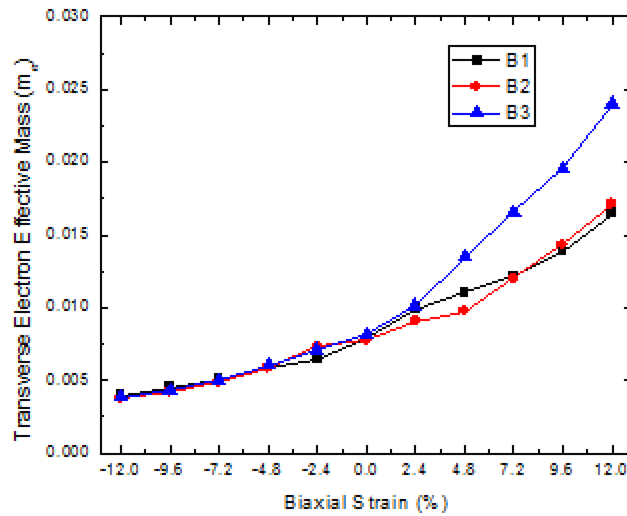

Figure 4.22: Transverse electron effective mass of B1, B2 and B3 as a function of percentage biaxial strain applied to the super lattice.

4.3.4.2 Hole Effective Mass

The longitudinal hole effective mass is the mass considered in Γ to K direction. It is clear from Fig. 4.23 that there is almost negligible change among the longitudinal effective masses of three configurations in compressive region. In tensile region B1 and B2 increases almost similarly but B3 shows a rapid increase in effective mass with the increase of tensile strain. The transverse hole effective mass also shows the same trend like longitudinal hole effective mass as shown in Fig. 4.24.

The reason behind the results can be explained from Fig. 4.11. It is seen that the curvature of all valence band maxima increase with compressive strain. The effective mass of hole is inversely proportional to the curvature of the band near band maxima. Hence higher curvature creates lower effective mass (both longitudinal and transverse) for all the configurations of C/h-BN HBL. Here longitudinal effective mass means the mass in Γ to K direction and the transverse effective mass is taken in the direction perpendicular to the Γ to K in k-space.

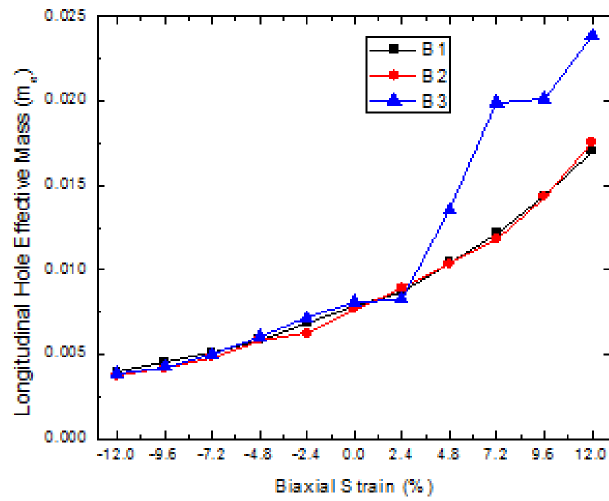

Figure 4.23: Longitudinal hole effective mass of B1, B2 and B3 as a function of percentage biaxial strain applied to the super lattice.

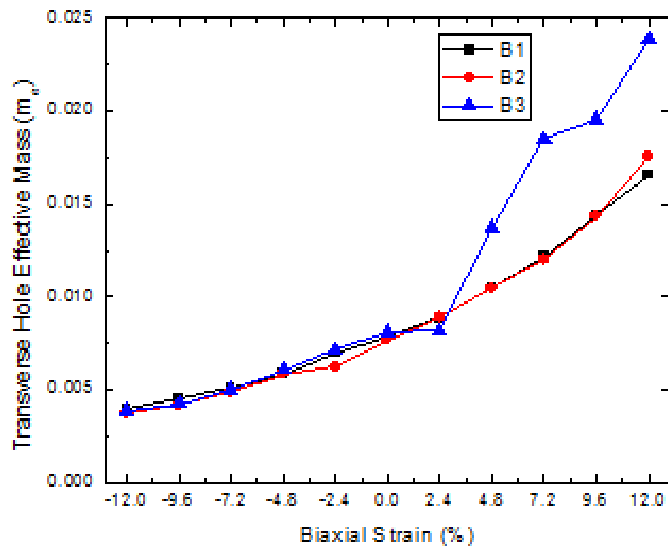

Figure 4.24 Transverse hole effective mass of B1, B2 and B3 as a function of percentage biaxial strain applied to the super lattice.

4.3.5 Fermi Velocity

4.3.5.1 Electron Fermi Velocity

The electron Fermi velocity for B1, B2 and B3 structures is shown in Fig. 4.25. The Fermi velocity for optimized B1 structure was found to be 0.855×10^6 m/s, closely matched with 0.8×10^6 m/s reported by [63]. For optimized B2 and B3 structure the value is 0.843×10^6 m/s and 0.840×10^6 m/s respectively.

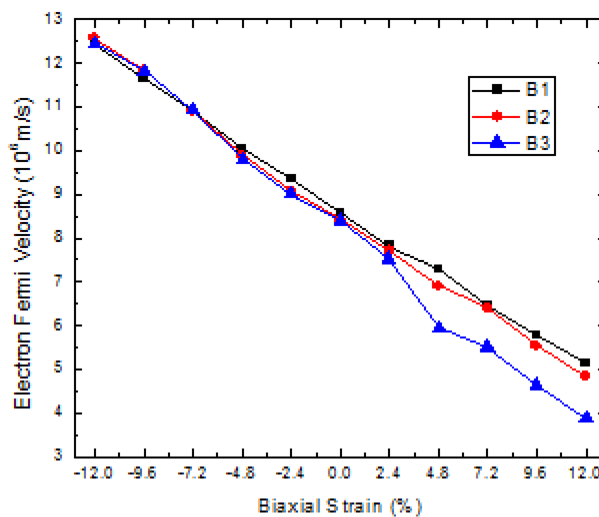

Figure 4.25 Electron Fermi velocity of B1, B2 and B3 as a function of percentage biaxial strain applied to the super lattice

Electron Fermi velocity decreases from compressive to tensile strain. It is also observed that all the three structures have almost same Fermi velocity as long as compressive strain is considered. In tensile strain the velocity for B3 structure decreases more rapidly than B1 and B2. The reason behind the results can be explained from Fig. 4.11. It is observed that the slope of the bands near band minima increases with compressive strain. The Fermi velocity is directly proportional to the slope near band edge. Hence higher slope in compressive region creates higher Fermi velocity. Higher Fermi velocity is very crucial for electronic device application.

4.3.5.2 Hole Fermi Velocity

The hole also shows almost same behavior in terms of Fermi velocity. The hole Fermi velocity for relaxed B1, B2 and B3 configurations are 0.853×10^6 m/s, 0.845×10^6 m/s and 0.823×10^6 m/s respectively. The hole Fermi velocity also show similar characteristic as electron Fermi velocity.

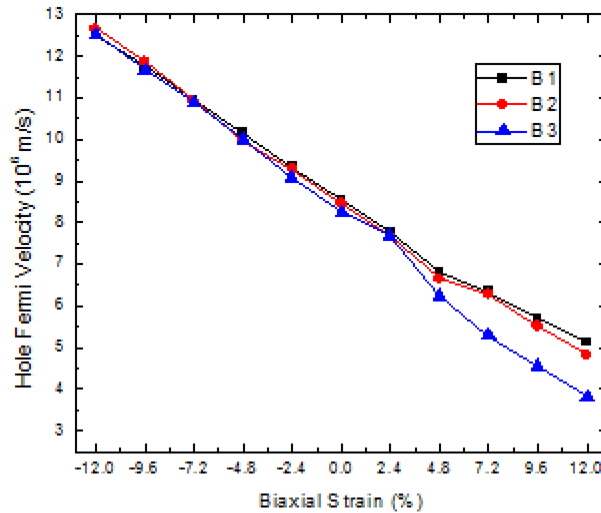

Figure 4.26: Hole Fermi velocity of B1, B2 and B3 as a function of percentage biaxial strain applied to the super lattice

The reason behind the results can be explained from Fig. 4.11. It is observed that the slope of the bands near valence band maxima increases with compressive strain. The Fermi velocity is directly proportional to the slope near band edge. Hence higher slope in compressive region creates higher Fermi velocity. Higher Fermi velocity is very crucial for electronic device application. It plays a significant role in ambipolar transport in two dimensional materials. So this result will be helpful in further research in ambipolar transport in electronic, optoelectronic and photonic devices as well.

Chapter 5

Transport Performance: Ballistic MOSFET

In this chapter the transport performance of a top gate ballistic MOSFET was investigated by applying various biaxially strained C/h-BN HBL material in the channel and observing the IV characteristics curve. Finally, the configuration with maximum available band gap was used as channel material and transport performance was observed.

5.1 Basic Device Structure

Fig. 5.1 shows the schematic device structure of the planar 2-D C/h-BN FET considered for our studies. This device is a prototype device to investigate the effect of biaxial strain on transport performance. The channel length (L_{ch}) and width (W) considered in our simulation is 30Å and 20Å respectively. High-κ HfO2 of 5Å thickness is chosen as the gate dielectric. Work function of metal in gate and both drain and source are considered to be same. X(A) direction is in the perpendicular to the channel and Z(C) is in the direction of the channel whereas Y(B) is in the direction of width of the MOSFET.

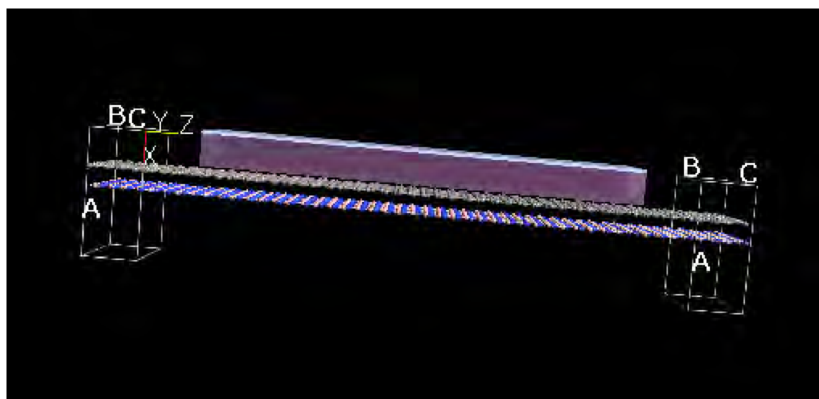

Figure 5.1: Basic device structure of C/h-BN channel ballistic MOSFET.

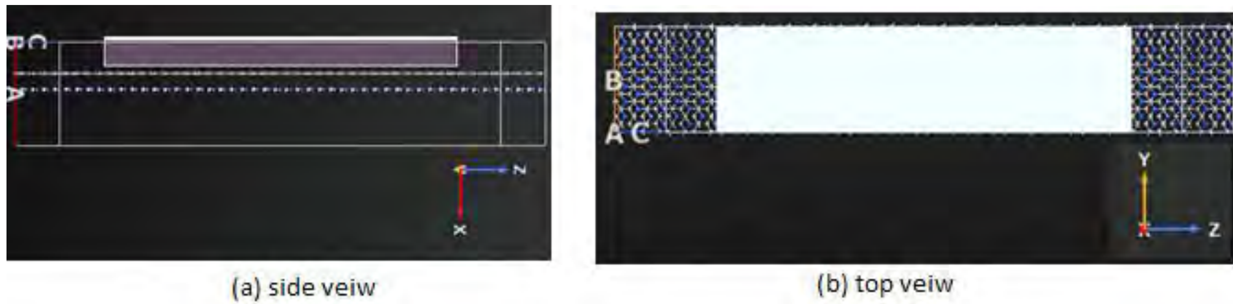

Figure 5.2: Basic device structure of C/h-BN channel ballistic MOSFET

5.2 IV Characteristics

In this section, the effects of biaxial strain on current voltage (I-V) characteristics of the top gate ballistic MOSFET are presented. In Fig. 5.3 IV characteristics for B1, B2 and B3 are shown. It is clear that in relaxed condition there is negligible variation in IV characteristics with change in configuration of C/h-BN HBL. This may be explained as the difference in band gap is very negligible for the relaxed configurations.

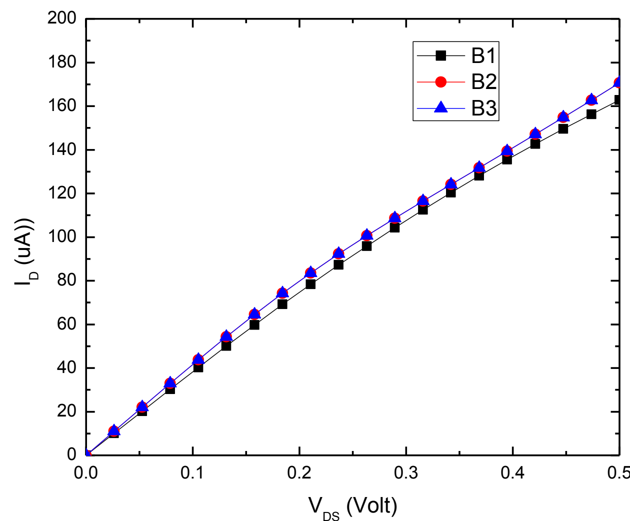

Figure 5.3: IV characteristics curve for relaxed structures of B1, B2 and B3

5.2.1 Effect of Strain (B1 Configuration)

Fig. 5.4 shows that for B1 structure drain current increases from compressive to tensile strain.Current is minimum for the relaxed structure. There is no saturation achieved with the application of drain to source voltage for various strained B1 configurations. If the drain to source voltage is further increased there is the same increasing trend in the IV curve which is also observed in graphene. The reason may be the small band gap created by application of biaxial strain in this configuration.

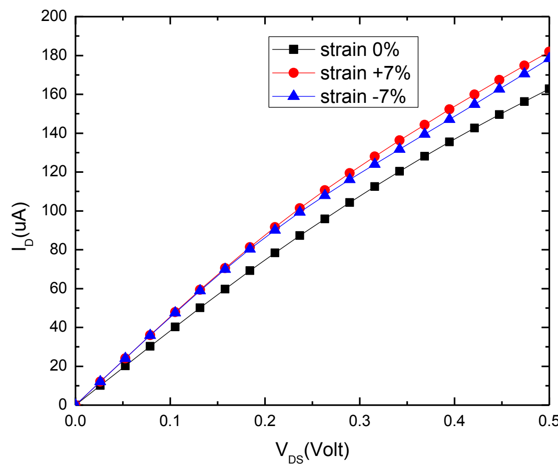

Figure 5.4: Effect of biaxial strain on I-V characteristics for B1 configuration based MOSFET

5.2.2 Effect of Strain (B2 Configuration)

It is evident from Fig. 5.5 that for B2 configuration drain current increases from tensile to compressive strain. The relaxed structure has current in between compressive and tensile region.

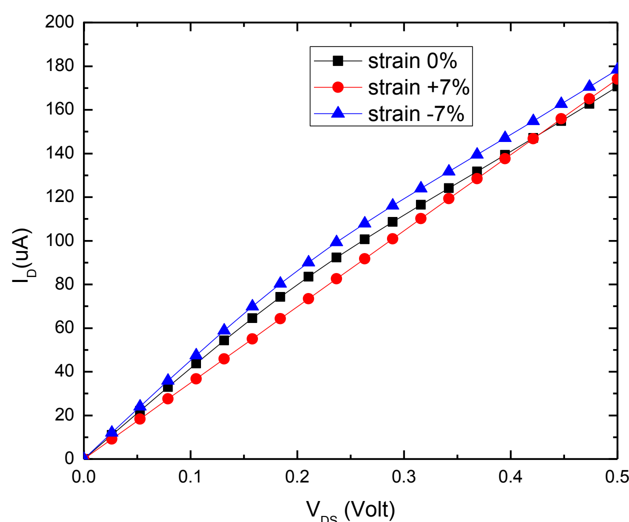

Figure 5.5: Effect of biaxial strain on I-V characteristics for B2 configuration based MOSFET

There is no saturation achieved with the application of drain to source voltage for various strained B2 configurations either. If the drain to source voltage is further increased there is the same increasing trend in the IV curve which is also observed in graphene. The reason may be the small band gap created by application of biaxial strain in this configuration.

5.2.3 Effect of Strain (B3 Configuration)

B3 structure shows similar characteristics of transport as B2. From Fig. 5.6 it is also observed that the IV curve shows no saturation. There is no saturation achieved with the application of drain to source voltage for various strained B3 configurations upto 7% tensile strain. If the drain to source voltage is further increased there is the same increasing trend in the IV curve which is also observed in graphene. The reason may be

the small band gap created by application of biaxial strain upto 7% strain in this configuration.

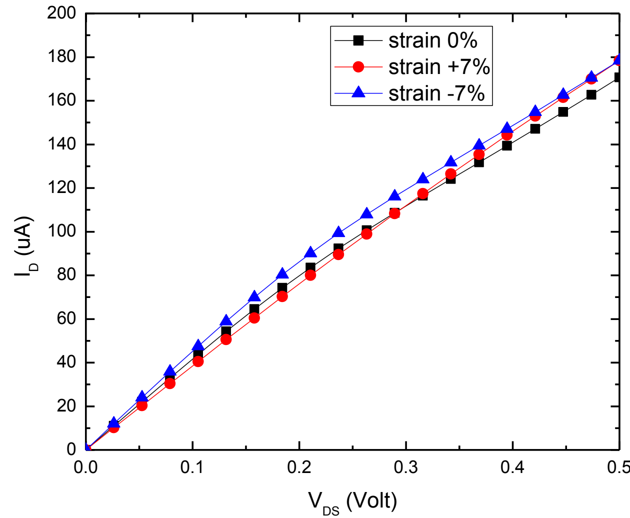

Figure 5.6: Effect of biaxial strain on I-V characteristics for B3 configuration based MOSFET

5.3 Optimum Channel Material for Ballistic MOSFET

From chapter 4 we came to know that 12% tensile strained B3 configuration has highest band gap ever possible in any C/h-BN bilayer system and the band gap in B3 increases with tensile strain. So to design a MOSFET with a channel material with considerable band gap, we have to choose the material from higher tensile strained configuration of B3. To further investigate the scenario, we measured the drain current at a particular dran to source voltage for tensile strained B3 configuration which is shown in Fig. 5.7

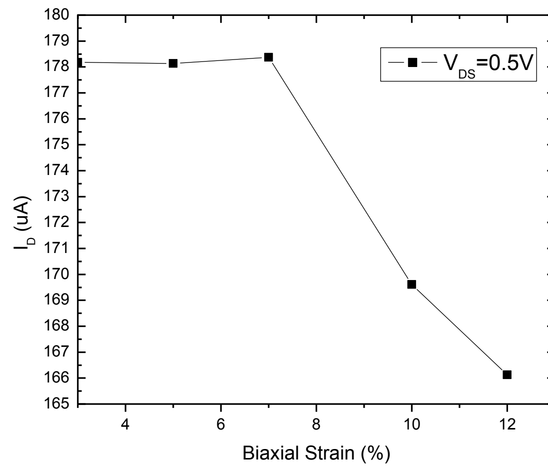

Figure 5.7: Drain current at a particular drain voltage is plotted as a function of percentage biaxial strain for B3 configuration. Here V_{DS}=0.5V.

From Fig. 5.7 it is clear that the drain current tends to reach saturation with the application of tensile strain. So 12% tensile strained B3 would be a better choice for channel material in MOSFET application. And interestingly we have got the drain current saturation with this material applied as channel in a MOSFET shown in Fig. 5.8. It is also observed that with the application of gate voltage the current drive current in the channel decreases for a particular drain to source voltage. This implies the depletion mode operation of the MOSFET.

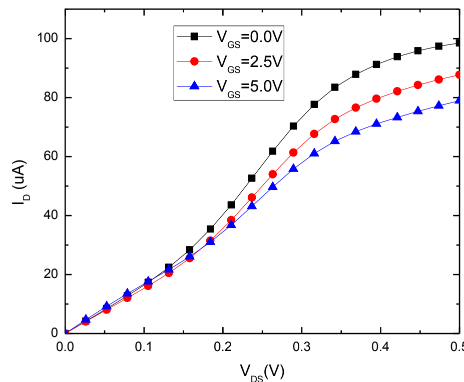

Figure 5.8: IV characteristics curve with 12% tensile strained B3 in channel of MOSFET

Chapter 6

Conclusion

6.1 Summary

We investigated two dimensional C/h-BN hetero bilayer (HBL) systems with all its possible configurations such as B1, B2 and B3 (configurations depend on the relative orientation of atoms in the planes). Atomic and structural optimization was done to relax the configurations and the optimum lattice parameter and interlayer distance for the configurations are obtained. Then with these parameter value, DFT under LDA using PZ pseudo potential was applied to calculate the electronic band structure and DOS. Then some important material electronic parameter like carrier effective mass, band gap and Fermi velocity were determined. Our results from structure optimization show very good agreement with the reported results in literature. From the band structure it was observed that relaxed B3 has the highest and B2 has the lowest band gap. By applying tensile strain the band gap can be further increased for all the configurations as observed in our simulation results. Effective mass also shows the same trend as the band gap, increases with the application of tensile strain. But Fermi velocity showed the opposite trend, decreases with tensile strain, the reason was discussed in the result section of this work. From DOS it was observed, that the gap in near Fermi line is almost equal to the band gap, in conformity with the concept discussed in literature. The linear shape in low energy region in integrated DOS shows the graphene like characteristics in this bilayer material system. It was also observed that for higher compressive strain the integrated DOS reaches saturation which is the outcome of the reduction in DOS for higher energy.

Finally, we applied various strained systems of C/h-BN HBL in channel material of a top gate ballistic MOSFET and observed that there is no saturation reached for B1 and B2 configurations and also up to 7% tensile strain for B3 configuration. We also observed that with the increase in band gap the drive current tends to decrease and finally for 12% tensile strain saturation in drive current is achieved. Ultimately, gate voltage was varied and found that it decreases the drive current, a behavior similar to depletion mode MOSFET.

6.2 Suggestion for Future Works

This work can facilitate further study with this material system and device structure. The suggestions for future work are as follows:

- In this work LDA approximation was used in determining band structure. Though it calculates the band curvature exactly, it underestimates the band gap. Hence GW method can be developed and applied in this system for a better result.
- Monolayer graphene and single layer BN was used in this work. The number of layer in graphene and/or the number of layer in BN can be increased and observed the effects on electronic structure.
- Sandwiched structure like one graphene layer between two BN or one BN between two graphene layer can also be investigated.
- In this work prototype device structure was considered due to the huge simulation time and resource required for a more realistic MOSFET simulation in atomistic level. Analytical expressions can be developed for realistic MOSFET for easier simulation and understanding of the underlying physics in atomistic MOSFET.
- Biaxial strain dependent electronic structure was calculated in the bilayer system. Recent studies have shown that a band gap can be opened in bilayer graphene by applying electric field in perpendicular direction to the plane. So the effect of electric field on the electronic structure of this bilayer material can also be investigated.

References

[1] Schwierz, Frank, Hei Wong, and Juin J. Liou, eds. *Nanometer CMOS*. Pan Stanford Publishing, 2010.

[2] Schwierz, Frank, and Juin J. Liou. *Modern microwave transistors: theory, design, and performance*. Wiley-Interscience, 2003.

[3] Schwierz, Frank, and Juin J. Liou. "RF transistors: Recent developments and roadmap toward terahertz applications." *Solid-State Electronics* 51, no. 8 (2007): 1079-1091.

[4] Taur, Yuan, and Tak H. Ning. *Fundamentals of modern VLSI devices*. Vol. 2. Cambridge: Cambridge University Press, 1998.

[5] Wilk, Glen D., Robert M. Wallace, and J. M. Anthony. "High-κ gate dielectrics: Current status and materials properties considerations." *Journal of applied physics* 89, no. 10 (2001): 5243-5275.

[6] Ferain, Isabelle, Cynthia A. Colinge, and Jean-Pierre Colinge. "Multigate transistors as the future of classical metal-oxide-semiconductor field-effect transistors." *Nature* 479, no. 7373 (2011): 310-316.

[7] Frank, David J., Yuan Taur, and H-SP Wong. "Generalized scale length for two-dimensional effects in MOSFETs." *Electron Device Letters, IEEE* 19, no. 10 (1998): 385-387.

[8] Aberg, Ingvar, and Judy L. Hoyt. "Hole transport in UTB MOSFETs in strained-Si directly on insulator with strained-Si thickness less than 5 nm." *Electron Device Letters, IEEE* 26, no. 9 (2005): 661-663.

[9] Han, Melinda Y., Barbaros Özyilmaz, Yuanbo Zhang, and Philip Kim. "Energy band-gap engineering of graphene nanoribbons." *Physical review letters* 98, no. 20 (2007): 206805..

[10] Evaldsson, Martin, Igor V. Zozoulenko, Hengyi Xu, and T. Heinzel. "Edge-disorder-induced Anderson localization and conduction gap in graphene nanoribbons." *Physical Review B* 78, no. 16 (2008): 161407.

[11] Cervantes-Sodi, F., G. Csanyi, S. Piscanec, and A. C. Ferrari. "Edge-functionalized and substitutionally doped graphene nanoribbons: Electronic and spin properties." *Physical Review B* 77, no. 16 (2008): 165427.

[12] Castro, Eduardo V., K. S. Novoselov, S. V. Morozov, N. M. R. Peres, JMB Lopes Dos Santos, Johan Nilsson, F. Guinea, A. K. Geim, and AH Castro Neto. "Biased bilayer graphene: semiconductor with a gap tunable by the electric field effect." *Physical Review Letters* 99, no. 21 (2007): 216802.

[13] Gava, Paola, Michele Lazzeri, A. Marco Saitta, and Francesco Mauri. "Ab initio study of gap opening and screening effects in gated bilayer graphene." *Physical Review B* 79, no. 16 (2009): 165431.

[14] Ohta, Taisuke, Aaron Bostwick, Thomas Seyller, Karsten Horn, and Eli Rotenberg. "Controlling the electronic structure of bilayer graphene." *Science*313, no. 5789 (2006): 951-954.

[15] Zhang, Yuanbo, Tsung-Ta Tang, Caglar Girit, Zhao Hao, Michael C. Martin, Alex Zettl, Michael F. Crommie, Y. Ron Shen, and Feng Wang. "Direct observation of a widely tunable bandgap in bilayer graphene." *Nature* 459, no. 7248 (2009): 820-823.

[16] Rotenberg, Eli, Aaron Bostwick, Taisuke Ohta, Jessica L. McChesney, Thomas Seyller, and Karsten Horn. "Origin of the energy bandgap in epitaxial graphene." *Nature materials* 7, no. 4 (2008): 258-259.

[17] Zhou, S. Y., G-H. Gweon, A. V. Fedorov, P. N. First, W. A. De Heer, D-H. Lee, F. Guinea, AH Castro Neto, and A. Lanzara. "Substrate-induced bandgap opening in epitaxial graphene." *Nature materials* 6, no. 10 (2007): 770-775..

[18] Bostwick, Aaron, Taisuke Ohta, Thomas Seyller, Karsten Horn, and Eli Rotenberg. "Quasiparticle dynamics in graphene." *Nature Physics* 3, no. 1 (2006): 36-40.

[19] Peng, Xiangyang, and Rajeev Ahuja. "Symmetry breaking induced bandgap in epitaxial graphene layers on SiC." *Nano letters* 8, no. 12 (2008): 4464-4468.

[20] Pereira, Vitor M., AH Castro Neto, and N. M. R. Peres. "Tight-binding approach to uniaxial strain in graphene." *Physical Review B* 80, no. 4 (2009): 045401.

[21] Ni, Zhen Hua, Ting Yu, Yun Hao Lu, Ying Ying Wang, Yuan Ping Feng, and Ze Xiang Shen. "Uniaxial strain on graphene: Raman spectroscopy study and band-gap opening." *ACS nano* 2, no. 11 (2008): 2301-2305.

[22] Pan, Wei, Jianliang Xiao, Junwei Zhu, Chenxi Yu, Gang Zhang, Zhenhua Ni, K. Watanabe, T. Taniguchi, Yi Shi, and Xinran Wang. "Biaxial compressive strain engineering in graphene/boron nitride heterostructures." *Scientific reports* 2 (2012).

[23] Chen, Jian-Hao, Chaun Jang, Shudong Xiao, Masa Ishigami, and Michael S. Fuhrer. "Intrinsic and extrinsic performance limits of graphene devices on SiO2." *Nature nanotechnology* 3, no. 4 (2008): 206-209.

[24] Dean, C. R., A. F. Young, I. Meric, C. Lee, L. Wang, S. Sorgenfrei, K. Watanabe et al. "Boron nitride substrates for high-quality graphene electronics."*Nature nanotechnology* 5, no. 10 (2010): 722-726.

[25] Boehm, H. P., A. Clauss, G. O. Fischer, and U. Hofmann. "Dünnste kohlenstoff-folien." *Z. Naturforschg* 17 (1962): 150-157.

[26] May, John W. "Platinum surface LEED rings." *Surface Science* 17, no. 1 (1969): 267-270..

[27] Van Bommel, A. J., J. E. Crombeen, and A. Van Tooren. "LEED and Auger electron observations of the SiC (0001) surface." *Surface Science* 48, no. 2 (1975): 463-472.

[28] Novoselov, Kostya S., Andre K. Geim, S. V. Morozov, D. Jiang, Y_ Zhang, S. V. Dubonos, I. V. Grigorieva, and A. A. Firsov. "Electric field effect in atomically thin carbon films." *science* 306, no. 5696 (2004): 666-669.).

[29] Yang, Li, Cheol-Hwan Park, Young-Woo Son, Marvin L. Cohen, and Steven G. Louie. "Quasiparticle energies and band gaps in graphene nanoribbons."*Physical Review Letters* 99, no. 18 (2007): 186801.

[30] Kim, Kinam. "From the future Si technology perspective: Challenges and opportunities." In *Electron Devices Meeting (IEDM), 2010 IEEE International*, pp. 1-1. IEEE, 2010.

[31] Li, Xiaolin, Xinran Wang, Li Zhang, Sangwon Lee, and Hongjie Dai. "Chemically derived, ultrasmooth graphene nanoribbon semiconductors." *Science* 319, no. 5867 (2008): 1229-1232.

[32] Chen, Zhihong, Yu-Ming Lin, Michael J. Rooks, and Phaedon Avouris. "Graphene nano-ribbon electronics." *Physica E: Low-dimensional Systems and Nanostructures* 40, no. 2 (2007): 228-232.

[33] Jiao, Liying, Xinran Wang, Georgi Diankov, Hailiang Wang, and Hongjie Dai. "Facile synthesis of high-quality graphene nanoribbons." *Nature nanotechnology* 5, no. 5 (2010): 321-325.

[34] Raza, Hassan, and Edwin C. Kan. "Armchair graphene nanoribbons: electronic structure and electric-field modulation." *Physical Review B* 77, no. 24 (2008): 245434.

[35] Ni, Zhen Hua, Ting Yu, Yun Hao Lu, Ying Ying Wang, Yuan Ping Feng, and Ze Xiang Shen. "Uniaxial strain on graphene: Raman spectroscopy study and band-gap opening." *ACS nano* 2, no. 11 (2008): 2301-2305.

[36] Wang, Qing Hua, Kourosh Kalantar-Zadeh, Andras Kis, Jonathan N. Coleman, and Michael S. Strano. "Electronics and optoelectronics of two-dimensional transition metal dichalcogenides." *Nature nanotechnology* 7, no. 11 (2012): 699-712.

[37] Xue, Jiamin, Javier Sanchez-Yamagishi, Danny Bulmash, Philippe Jacquod, Aparna Deshpande, K. Watanabe, T. Taniguchi, Pablo Jarillo-Herrero, and Brian J. LeRoy. "Scanning tunnelling microscopy and spectroscopy of ultra-flat graphene on hexagonal boron nitride." *Nature materials* 10, no. 4 (2011): 282-285.

[38] Dean, C. R., A. F. Young, P. Cadden-Zimansky, L. Wang, H. Ren, K. Watanabe, T. Taniguchi, P. Kim, J. Hone, and K. L. Shepard. "Multicomponent

fractional quantum Hall effect in graphene." *Nature Physics* 7, no. 9 (2011): 693-696.

[39] Young, Andrea F., Cory R. Dean, Lei Wang, Hechen Ren, Paul Cadden-Zimansky, Kenji Watanabe, Takashi Taniguchi, James Hone, Kenneth L. Shepard, and Philip Kim. "Spin and valley quantum Hall ferromagnetism in graphene." *Nature Physics* 8, no. 7 (2012): 550-556.

[40] Dean, C. R., L. Wang, P. Maher, C. Forsythe, F. Ghahari, Y. Gao, J. Katoch et al. "Hofstadter/'s butterfly and the fractal quantum Hall effect in moire superlattices." *Nature* 497, no. 7451 (2013): 598-602.

[41] Ponomarenko, L. A., R. V. Gorbachev, G. L. Yu, D. C. Elias, R. Jalil, A. A. Patel, A. Mishchenko et al. "Cloning of Dirac fermions in graphene superlattices." *Nature* 497, no. 7451 (2013): 594-597.

[42] Hunt, B., J. D. Sanchez-Yamagishi, A. F. Young, M. Yankowitz, Brian J. LeRoy, K. Watanabe, T. Taniguchi et al. "Massive Dirac fermions and Hofstadter butterfly in a van der Waals heterostructure." *Science* 340, no. 6139 (2013): 1427-1430.

[43] Meric, I., Cory Dean, A. Young, J. Hone, Philip Kim, and Kenneth L. Shepard. "Graphene field-effect transistors based on boron nitride gate dielectrics." In*Electron Devices Meeting (IEDM), 2010 IEEE International*, pp. 23-2. IEEE, 2010.

[44] Dean, C. R., A. F. Young, I. Meric, C. Lee, L. Wang, S. Sorgenfrei, K. Watanabe et al. "Boron nitride substrates for high-quality graphene electronics."*Nature nanotechnology* 5, no. 10 (2010): 722-726.

[45] Neto, AH Castro, F. Guinea, N. M. R. Peres, Kostya S. Novoselov, and Andre K. Geim. "The electronic properties of graphene." *Reviews of modern physics*81, no. 1 (2009): 109.

[46] Peres, N. M. R. "Colloquium: The transport properties of graphene: An introduction." *Reviews of Modern Physics* 82, no. 3 (2010): 2673.

[47] Sarma, S. Das, and E. H. Hwang. "Conductivity of graphene on boron nitride substrates." *Physical Review B* 83, no. 12 (2011): 121405..

[48] Weitz, R. Thomas, and Amir Yacoby. "Nanomaterials: graphene rests easy."*Nature nanotechnology* 5, no. 10 (2010): 699-700.

[49] ing, Fei, Hengxing i, onghai hen, ndreas Herklotz, Kathrin rr, Yongfeng Mei, Armando Rastelli, and Oliver G. Schmidt. "Stretchable graphene: a close look at fundamental parameters through biaxial straining."*Nano letters* 10, no. 9 (2010): 3453-3458.

[50] Giovannetti, Gianluca, Petr A. Khomyakov, Geert Brocks, Paul J. Kelly, and Jeroen van den Brink. "Substrate-induced band gap in graphene on hexagonal boron nitride: Ab initio density functional calculations." *Physical Review B* 76, no. 7 (2007): 073103.

[51] Fan, Yingcai, Mingwen Zhao, Zhenhai Wang, Xuejuan Zhang, and Hongyu Zhang. "Tunable electronic structures of graphene/boron nitride heterobilayers."*Applied Physics Letters* 98, no. 8 (2011): 083103.

[52] Sławińska, ., I. Zasada, P. Kosiński, and Z. Klusek. "Reversible modifications of linear dispersion: Graphene between boron nitride monolayers." *Physical Review B* 82, no. 8 (2010): 085431.

[53] Ramasubramaniam, Ashwin, Doron Naveh, and Elias Towe. "Tunable band gaps in bilayer graphene− BN heterostructures." *Nano letters* 11, no. 3 (2011): 1070-1075.

[54] Li, Jin, Gui Gui, and Jianxin Zhong. "Tunable bandgap structures of two-dimensional boron nitride." *Journal of Applied Physics* 104, no. 9 (2008): 094311.

[55] Pereira, Vitor M., R. M. Ribeiro, N. M. R. Peres, and AH Castro Neto. "Optical properties of strained graphene." *EPL (Europhysics Letters)* 92, no. 6 (2010): 67001.

[56] Farjam, M., and H. Rafii-Tabar. " o mment on “Band structure engineering of graphene by strain: First-principles calculations”." *Physical Review B* 80, no. 16 (2009): 167401.

[57] Gui, Gui, Jin Li, and Jianxin Zhong. "Band structure engineering of graphene by strain: First-principles calculations." *Physical Review B* 78, no. 7 (2008): 075435.

[58] Choi, Seon-Myeong, Seung-Hoon Jhi, and Young-Woo Son. "Effects of strain on electronic properties of graphene." *Physical Review B* 81, no. 8 (2010): 081407.

[59] Mohiuddin, T. M. G., A. Lombardo, R. R. Nair, A. Bonetti, G. Savini, R. Jalil, N. Bonini et al. "Uniaxial strain in graphene by Raman spectroscopy: G peak splitting, Grüneisen parameters, and sample orientation." *Physical Review B* 79, no. 20 (2009): 205433.

[60] Huang, Mingyuan, Hugen Yan, Tony F. Heinz, and James Hone. "Probing strain-induced electronic structure change in graphene by Raman spectroscopy." *Nano letters* 10, no. 10 (2010): 4074-4079.

[61] Frank, Otakar, Marcel Mohr, Janina Maultzsch, Christian Thomsen, Ibtsam Riaz, Rashid Jalil, Kostya S. Novoselov et al. "Raman 2D-band splitting in graphene: theory and experiment." *Acs Nano* 5, no. 3 (2011): 2231-2239..

[62] Kim, Keun Soo, Yue Zhao, Houk Jang, Sang Yoon Lee, Jong Min Kim, Kwang S. Kim, Jong-Hyun Ahn, Philip Kim, Jae-Young Choi, and Byung Hee Hong. "Large-scale pattern growth of graphene films for stretchable transparent electrodes." *Nature* 457, no. 7230 (2009): 706-710.

[63] Behera, Harihar, and Gautam Mukhopadhyay. "Strain-tunable band gap in graphene/h-BN hetero-bilayer." *Journal of Physics and Chemistry of Solids* 73, no. 7 (2012): 818-821.

[64] Feynman, R. P. (1939), “Forces in molecules.” *Physical Review*, *56*(4), 340.

[65] P. Giannozzi et al., “QU N TUM ESPRESSO: a modular and opensourcesoftware project for quantum simulations of materials” . Phys.Condens. Matter, vol. 21, pp. 395502, 2009.

[66] Taylor, J., Guo, H., & Wang, J. (2001), “Ab initio modeling of quantum transport properties of molecular electronic devices,” *Physical Review B*, *63*(24), 245407.

[67] Brandbyge, Mads, José-Luis Mozos, Pablo Ordejón, Jeremy Taylor, and Kurt Stokbro. "Density-functional method for nonequilibrium electron transport."*Physical Review B* 65, no. 16 (2002): 165401.

[68] WANG, Zheng-chuan, and Bo-zang LI. "Born-Oppenheimer Approximation."

[69] Hohenberg, Pierre, and Walter Kohn. "Inhomogeneous electron gas." *Physical review* 136, no. 3B (1964): B864.

[70] Kohn, Walter, and Lu Jeu Sham. "Self-consistent equations including exchange and correlation effects." *Physical Review* 140, no. 4A (1965): A1133.

[71] Perdew, John P., and Alex Zunger. "Self-interaction correction to density-functional approximations for many-electron systems." *Physical Review B* 23, no. 10 (1981): 5048.

[72] Perdew, John P., and Wang Yue. "Accurate and simple density functional for the electronic exchange energy: Generalized gradient approximation." *Physical Review B* 33, no. 12 (1986): 8800.

[73] Perdew, John P., Kieron Burke, and Matthias Ernzerhof. "Generalized gradient approximation made simple." *Physical review letters* 77, no. 18 (1996): 3865.

[74] Zubko, Pavlo, Stefano Gariglio, Marc Gabay, Philippe Ghosez, and Jean-Marc Triscone. "Interface physics in complex oxide heterostructures." *Annu. Rev. Condens. Matter Phys.* 2, no. 1 (2011): 141-165.

[75] Phillips, James C. "Energy-band interpolation scheme based on a pseudopotential." *Physical Review* 112, no. 3 (1958): 685.

[76] Kleinman, Leonard, and James C. Phillips. "Crystal Potential and Energy Bands of Semiconductors. I. Self-Consistent Calculations for Diamond."*Physical Review* 116, no. 4 (1959): 880.

[77] K. Stokbro, J. Taylor,and M. Brandbyge, H. Guo, Springer, (Berlin), 2007. Lec ture Notes in Physics, 680, 2005.

[78] Haug, Hartmut, and Antti-Pekka Jauho. *Quantum kinetics in transport and optics of semiconductors*. Vol. 123. Springer, 2007.

[79] Datta, Supriyo. *Electronic transport in mesoscopic systems*. Cambridge university press, 1997.

[80] Petersen, Dan Erik, Hans Henrik B. Sørensen, Per Christian Hansen, Stig Skelboe, and Kurt Stokbro. "Block tridiagonal matrix inversion and fast transmission calculations." *Journal of Computational Physics* 227, no. 6 (2008): 3174-3190.

[81] Sørensen, Hans Henrik B., Per Christian Hansen, Dan Erik Petersen, Stig Skelboe, and Kurt Stokbro. "Krylov subspace method for evaluating the self-energy matrices in electron transport calculations." *Physical Review B* 77, no. 15 (2008): 155301.

[82] Sørensen, Hans Henrik B., Per Christian Hansen, Dan Erik Petersen, Stig Skelboe, and Kurt Stokbro. "Efficient wave-function matching approach for quantum transport calculations." *Physical Review B* 79, no. 20 (2009): 205322.

[83] Lee, Yi-Hsien, Xin-Quan Zhang, Wenjing Zhang, Mu-Tung Chang, Cheng-Te Lin, Kai-Di Chang, Ya-Chu Yu et al. "Synthesis of Large-Area MoS2 Atomic Layers with Chemical Vapor Deposition." *Advanced Materials* 24, no. 17 (2012): 2320-2325.

[84] Effective Mass Calculator, A. Fonari, C. Sutton, (2012).

[85] Fan, Yingcai, Mingwen Zhao, Zhenhai Wang, Xuejuan Zhang, and Hongyu Zhang. "Tunable electronic structures of graphene/boron nitride heterobilayers."*Applied Physics Letters* 98, no. 8 (2011): 083103.

[86] Sławińska, ., I. Zasada, and Z. Klusek. "Energy gap tuning in graphene on hexagonal boron nitride bilayer system." *Physical Review B* 81, no. 15 (2010): 155433.

[87] Kokalj, Anton. "XCrySDen—a new program for displaying crystalline structures and electron densities." *Journal of Molecular Graphics and Modelling* 17, no. 3 (1999): 176-179.

[88] Yunkai Zhou Yousef Saad James R. Chelikowsky Tzu-Liang Chan, Murilo L. Tiago. Efficient algorithms for the electronic structure of nanocrystals, 2008. http://www:mcc:uiuc:edu/workshops/electronicstructure/2008/talks/04chant.pdf

Appendix

A. Flow Diagram on Algorithm to solve Kohn-Sham Equation

The basic algorithm of Kohn-Sham equation is presented here in flow chart form.

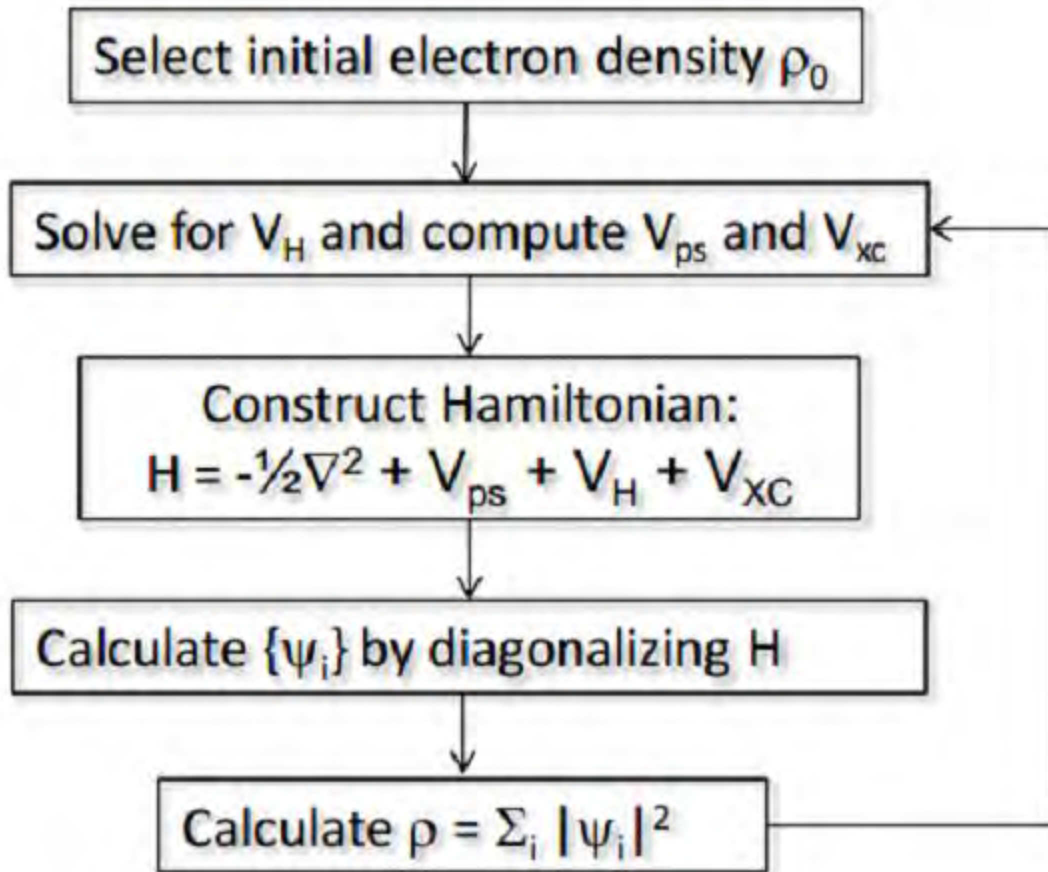

Figure A.1: A flow chart of algorithm to solve Kohn-Sham equation [88]